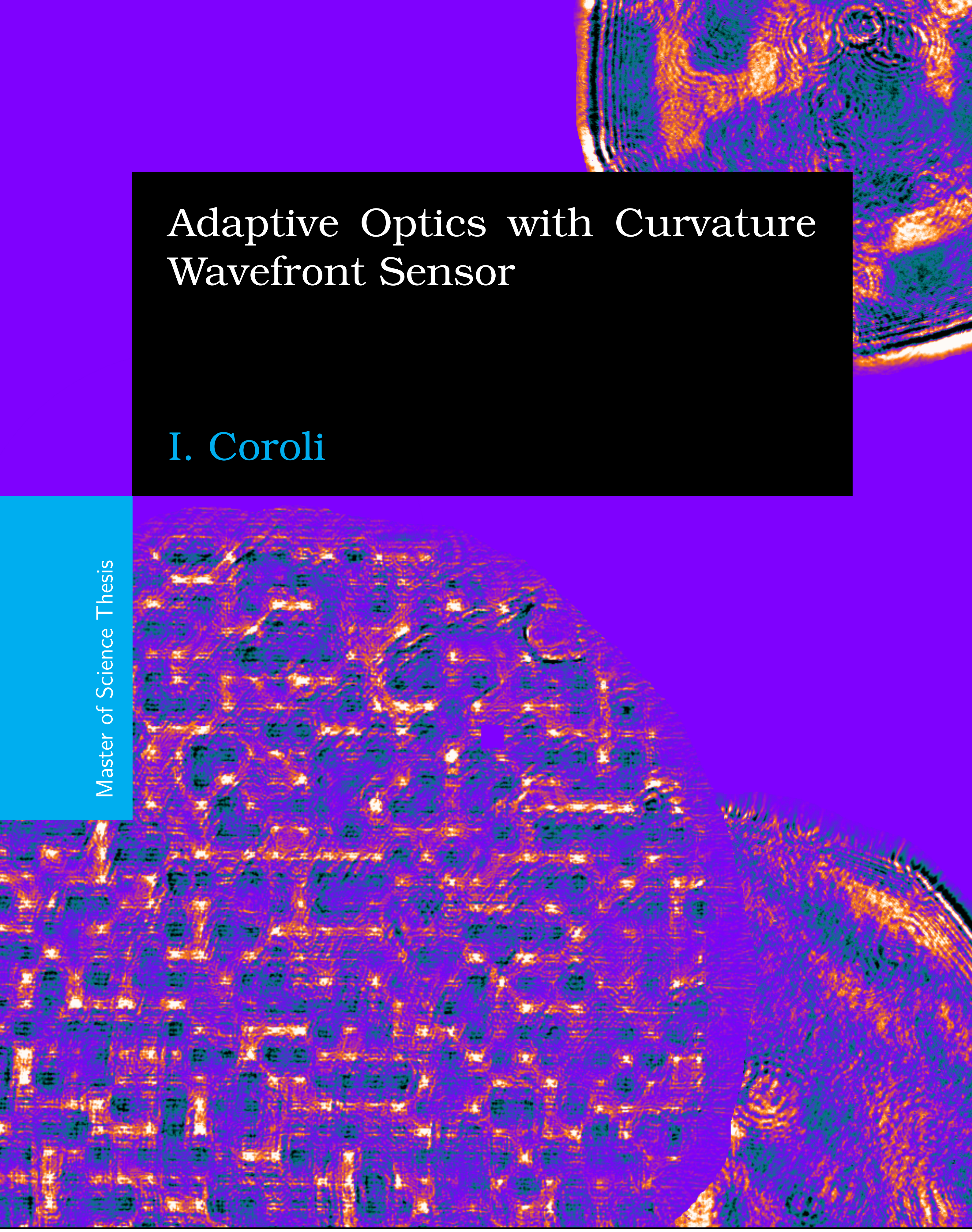

Adaptive Optics with Curvature Wavefront Sensor

I. Coroli

Master of Science Thesis

Delft University of Technology

Delft Center for Systems and Control

Adaptive Optics with Curvature Wavefront Sensor

Master of Science Thesis

For the degree of Master of Science in Systems and Control at Delft University of Technology

I. Coroli

September 4, 2018

Faculty of Mechanical, Maritime and Materials Engineering (3mE) · Delft University of Technology

DELFT UNIVERSITY OF TECHNOLOGY
DEPARTMENT OF
DELFT CENTER FOR SYSTEMS AND CONTROL (DCSC)

The undersigned hereby certify that they have read and recommend to the Faculty of Mechanical, Maritime and Materials Engineering (3mE) for acceptance a thesis entitled

ADAPTIVE OPTICS WITH CURVATURE WAVEFRONT SENSOR

by

I. COROLI

in partial fulfillment of the requirements for the degree of

MASTER OF SCIENCE SYSTEMS AND CONTROL

Dated: September 4, 2018

Supervisor(s): Prof.dr. G.V.Vdovin

Dr. P. Pozzi

Reader(s): Prof.dr.ir. M. Verhaegen

Dr. J. Kalkman

Dr. O.A. Krasnov

Abstract

When acquiring information using imaging techniques, one wants to achieve the best possible resolution in order to obtain valuable results. In the ideal scenario the size of the smallest resolved object features is limited by the wave properties of light, with a number of techniques developed to overcome this limit. In real life measurements the image quality is additionally deteriorated by the non-uniformities in refractive index along the beam propagation path, called aberrations. Adaptive Optics, introduced in 1950's independently by Horace Babcock and Vladimir Linnik is a set of methods used to overcome the effect of aberrations and thus improve the image quality. Initially used in military applications for tracking satellites, it later found civilian applications as advances in computing made it practical.

Adaptive Optics use principles of feedback control to correct aberrations, and thus a measurement of controlled variable is required. The most commonly measured quantity is first derivative of wavefront provided by the Shack-Hartmann sensor. Another possibility is to measure wavefront Laplacian, i.e. curvature, using the sensor proposed by Roddier in 1988. With the correct use of this sensor the deformable mirror actuators are decoupled from each other, enabling fast and accurate control of high order systems and potentially analog feedback loop.

In this thesis, the Roddier curvature wavefront sensor is studied. A number of modifications in the original sensor geometry and operating principles are made in order to make the system more robust and easy to implement in laboratory environment. Performance of the modified curvature wavefront sensor is evaluated in both simulation environment and physical setup. Finally, application of the curvature sensor to measure wind velocity is demonstrated.

Acknowledgements

I would like to thank my supervisor Gleb Vdovin for the opportunity to work on the exciting topic of this thesis, support throughout the research and a great introduction to a wider AO scientific community outside the university walls. I would like to thank Paolo Pozzi for developing in me a strange and unexplainable attraction towards rooms without the sunlight and big tables with holes, and for teaching me how to survive building optical setups. A special gratitude goes to my family who gave me the chance to study at TU Delft, and friends, who made the time outside studying unforgettable.

Delft, University of Technology I. Coroli
September 4, 2018

Chapter 1

Introduction

1-1 General Introduction

Imaging is a commonly used technique to extract information about object of interest. A huge benefit is that data is presented in form of an image, a very natural way for human beings. Since relatively big features can be easily perceived by the eye without using any additional instruments, a natural desire is to resolve objects as small as possible. In optical imaging in ideal conditions the size of the smallest resolvable features is determined by the wave properties of light, and is given by the diffraction limit. However, real life experiments are usually far from the theoretical limit of resolving power. Even if the imaging system is perfectly engineered, image resolution is additionally deteriorated by the inhomogeneities of optical refraction index along the beam path, which result in aberrations. Effectively, the aberrations deform surface of constant phase, Wavefront (WF) of incoming light wave, from ideal shape (sphere or plane).

In order to improve the imaging techniques, effect of aberrations must be corrected. Adaptive Optics (AO) presents a set of techniques to improve the image quality by pushing the WF shape as close as possible to the ideal one. The device that is used to manipulate WF shape is usually a Deformable Mirror (DM) or a Spatial Light Modulator (SLM). AO was introduced in 1950's by Horace Babcock [1] and later independently by Vladimir Linnik [2]. The original application was to monitor enemy satellites during the cold war. When high computational power became widely available, AO found other applications in civilian science and engineering, including biology, astronomy, and others.

Being essentially a feedback control technique, AO relies on measurements or estimates of controllable quantity. Most widely used is the first derivative of incoming WF, and the sensor that provides this measurement is Shack-Hartmann (SH) Wavefront Sensor (WFS). Although easy to implement and robust, the DM actuators usually produce nonlocal and coupled response with this type of sensor. The computational complexity of such setup grows quadratically with the number of actuators, and soon becomes an issue in high order systems. Additionally, for efficient control the minimal number of sensor outputs must be at least the number of controlled actuators, and in practice should be much larger, which is another problem for SH WFS.

An alternative is the Curvature Sensor (CS), proposed in 1988 by Roddier. It consists of two CCD cameras measuring intensity in slightly displaced planes, from which it is possible to derive Laplacian of WF. The response of mirror actuators with this type of sensor becomes local, and only one sensor output is needed to control each actuator. It additionally provides high resolution sampling of phase Laplacian, since the number of samples is effectively equivalent to the number of camera pixels inside the area of interest. As a result, CS can be coupled with high order mirrors, where SH WFS becomes hard to use.

This thesis is focused on studying Curvature Sensor (CS), implementing it in simulations and laboratory setup for a 96-channel DM and for a high order 952-channel DM.

1-2 Objectives

The main motivation of the thesis is to evaluate the performance and feasibility of using Curvature Sensor in adaptive optics with high order DM. The objectives therefore are:

1. Understand theoretical background of Wavefront curvature measurement. A number of papers was published on this type of WFS and on phase retrieval from curvature measurements, and some results from these sources are adapted and reported.
2. Perform modifications of the given sensor type in order to increase its robustness and make it easy to implement in laboratory setup.
3. Perform simulations of the CS-based adaptive optics in order to observe the expected properties of the system.
4. Implement CS-based adaptive optics setup in laboratory environment and test the performance.

1-3 Report structure

This report is structured as follows:

- **Chapter 2**: This is the first chapter from the main part of the report. Relevant theoretical preliminaries of light propagation in medium are given. Basic principles of optical image formation are explained. Adaptive optics as a tool to correct aberrations is introduced. Finally, a section is devoted to the studied Curvature Sensor.

- **Chapter 3**: In this chapter details about performed simulations are given, such as calculations of mirror influence functions, simulation of Shack-Hartmann sensor, simulation of atmospheric turbulence phase screen with Zernike statistics. Information about the experimental setup used to validate the method is given. A modification of the original Curvature Sensor is proposed and explained and a number of simulations and experiments is performed to test its behavior. Finally, an application of CS to measure wind velocity is shown.
- **Chapter 4**: In this final chapter the work done during the Master thesis is summarized and the results are discussed.

Chapter 2

Theoretical background

In this chapter necessary theoretical background is given. Propagation of optical fields in media is characterized using Helmholtz equation. From it Intensity Transport Equation (ITE) is derived. The basic ideas of image formation are given, and the principles of Adaptive Optics (AO) are explained.

2-1 Propagation equations

2-1-1 Helmholtz equation for scalar fields

In simulations of optical setups incoming field amplitude and phase is commonly assumed to be known, and the quantity of interest is field amplitude and phase at some other plane. To evaluate that, one needs to know how field propagates in the given environment. This is a well-studied problem. In a linear homogeneous isotropic media any complex component $U(x, y, z)$ of electromagnetic field satisfies the scalar Helmholtz equation [3]:

$$\nabla^2 U(x, y, z) + |k|^2 U(x, y, z) = 0, \tag{2-1}$$

where $k = \frac{2\pi}{\lambda}$ is the wave number in the media, ∇^2 is Laplace operator,

$$\nabla^2 = \sum_{i=1}^{3} \frac{\partial^2}{\partial x_i^2}.$$

The media is assumed to be non-absorbing and the wave number is thus real. Given completely defined $U(x, y, 0)$ in plane $z = 0$, Equation (2-1) expresses $U(x, y, z)$ at arbitrary z as a function of $U(x, y, 0)$. Let the field at plane $z = 0$ be $U(x, y, 0)$ and its 2-dimensional Fourier transform be denoted by $A(f_x, f_y, 0)$. By definition of Fourier transform [4],

$$U(x,y,0) = \int\int A(f_x,f_y,0)e^{i2\pi(f_x x+f_y y)}df_x df_y, \tag{2-2}$$

where f_x, f_y are spatial frequencies. By direct comparison to the plane wave decomposition it follows that $k_x = 2\pi f_x$, $k_y = 2\pi f_y$. Substitution of Equation (2-2) into Equation (2-1) yields the propagation equation for Fourier components of the field:

$$\frac{\partial^2 A}{\partial z^2} = -(k^2 - (2\pi f_x)^2 - (2\pi f_y)^2)A. \tag{2-3}$$

The solution to this equation takes form

$$A(f_x,f_y,z) = A(f_x,f_y,0)e^{i\sqrt{k^2-k_x^2-k_y^2}z}. \tag{2-4}$$

In a linear homogeneous isotropic media, the propagation of field component over a distance z corresponds to multiplication of Fourier transform of the field by $e^{i\sqrt{k^2-k_x^2-k_y^2}z}$. In this report only propagation in free space is relevant, for which $k = \frac{2\pi}{\lambda_0}$, where λ_0 is the wavelength in vacuum. The complex exponent in Equation (2-4) is free space transfer function:

$$H(k_x,k_y) = e^{i\sqrt{k_0^2-k_x^2-k_y^2}z}, \tag{2-5}$$

In order to simulate propagation of a given field $U(x,y,0)$ from plane $z = 0$ to $z = z_0$, the following steps are taken:

1. Calculate the Fourier transform of the field, $A(f_x,f_y,0) = \mathcal{F}\{U(x,y,0)\}$,
2. Use Equation (2-4) to obtain $A(f_x,f_y,z_0)$,
3. Calculate the inverse Fourier transform to obtain the field $U(x,y,z_0) = \mathcal{F}^{-1}\{A(f_x,f_y,z_0)\}$.

Assume now that paraxial approximation holds and the field propagates mostly in the positive z-direction. Then the solution takes the form $U(x,y,z) = u(x,y,z)e^{ikz}$ [5], where $u(x,y,z)$ is called reduced amplitude. Substitution of this form into Equation (2-1) yields

$$\frac{\partial^2 u}{\partial x^2} + \frac{\partial^2 u}{\partial y^2} + \frac{\partial^2 u}{\partial z^2} + 2ik\frac{\partial u}{\partial z} = 0. \tag{2-6}$$

For the fields that mainly propagate in the z-direction, the z-variations of u are mainly due to diffraction and are much slower compared to the variations in x- and y-directions, that are due to the finite size of the aperture. Thus the term $\frac{\partial^2 u}{\partial z^2} \ll \frac{\partial^2 u}{\partial x^2}, \frac{\partial^2 u}{\partial y^2}, 2k\frac{\partial u}{\partial z}$ is neglected.

Substituting $u(x,y,z) = U(x,y,z)e^{-ikz}$ into the resulting paraxial Helmholtz equation leads to:

$$(\frac{\partial^2}{\partial x^2} + \frac{\partial^2}{\partial y^2} + 2ik\frac{\partial}{\partial z} + 2k^2)U(x,y,z) = 0. \tag{2-7}$$

This form of paraxial Helmholtz equation is further used to derive Intensity Transport Equation (ITE).

2-1-2 Intensity Transport Equation

Optics deals with visible part of electromagnetic spectrum, for which typical frequencies are approximately in the range between $4 \cdot 10^{14}\,\mathrm{s}^{-1}$ and $7.5 \cdot 10^{14}\,\mathrm{s}^{-1}$. The response times of most of modern detectors is not small enough to measure phase of optical fields [6], and the measured quantity is energy averaged over many periods of light wave oscillations, i.e. intensity. This is a motivation for deriving a propagation equation for field intensity, similarly to how Equation (2-1) describes propagation of complex field amplitude.

Let complex field $U(\mathbf{r})$ be denoted by

$$U(\mathbf{r}) = (I(\mathbf{r}))^{1/2}\, e^{i\phi(\mathbf{r})}, \tag{2-8}$$

where $I(\mathbf{r}) \in \mathbb{R}_{\geq 0}$ is the intensity of the field, and $\phi(\mathbf{r}) \in \mathbb{R}$ is phase of the field. Begin with paraxial Helmholtz equation (2-7),

$$\left(i\frac{\partial}{\partial z} + \frac{\nabla_\perp^2}{2k} + k\right) U(\boldsymbol{r}) = 0, \tag{2-9}$$

where $\nabla_\perp$ denotes Laplace operator over transverse coordinates, $\nabla_\perp = \frac{\partial^2}{\partial x^2} + \frac{\partial^2}{\partial y^2}$. Since the intensity is defined as $I(\mathbf{r}) = U^*(\mathbf{r})U(\mathbf{r})$, the idea is to substitute Equation (2-8) into Equation (2-9), and left-multiply Equation (2-9) with complex conjugate of Equation (2-8):

$$\begin{aligned} U^*(\mathbf{r}) \left(i\frac{\partial}{\partial z} + \frac{\nabla_\perp^2}{2k} + k\right) U(\boldsymbol{r}) &= (I(\mathbf{r}))^{1/2} e^{-i\phi(\mathbf{r})} \left(i\frac{\partial}{\partial z} + \frac{\nabla_\perp^2}{2k} + k\right) (I(\mathbf{r}))^{1/2} e^{i\phi(\mathbf{r})} \\ &= i\frac{1}{2}I_z - I\phi_z + \frac{1}{2k}[\frac{1}{2}I_{xx} - \frac{1}{4}I^{-1}I_x^2 + iI_x\phi_x - I\phi_x^2 + iI\phi_{xx}] \\ &\quad + \frac{1}{2k}[\frac{1}{2}I_{yy} - \frac{1}{4}I^{-1}I_y^2 + iI_y\phi_y - I\phi_y^2 + iI\phi_{yy}] + kI = 0. \end{aligned} \tag{2-10}$$

Equation (2-10) consists of two equations, one for real and one for imaginary part. Taking imaginary part results in the Intensity Transport Equation (ITE):

$$I\nabla_{\perp}^{2}\phi = -k\frac{\partial I}{\partial z} - \nabla_{\perp} I \cdot \nabla_{\perp}\phi. \tag{2-11}$$

Since the intensity can be measured (for instance, by a CCD camera), $I(\mathbf{r})$ is known and the ITE becomes a linear equation and can be solved for $\phi(\mathbf{r})$. The equation can be further simplified under assumption of known constant intensity within the sharp round beam footprint in one plane,

$$I(\mathbf{r}) = I_0 H(r - r_0), \tag{2-12}$$

where $H(r-a)$ is the Heaviside step function, r_0 is the aperture radius and $I_0 > 0$. Constant intensity within the beam footprint is an oversimplification, but a common assumption made in adaptive optics. Upon substitution of Equation (2-12) into Equation (2-11), the equation becomes

$$I_0 H(r - r_0)\nabla^2\phi = -k\frac{\partial I}{\partial z} - I_0\delta(r - r_0)\frac{\partial \phi}{\partial r},$$

where $\delta(r - r_0)$ is the Dirac delta-function. It was assumed that the intensity gradient has only radial component:

$$\begin{aligned}\boldsymbol{\nabla} I(\mathbf{r}) &= \frac{\partial I}{\partial r}\hat{\mathbf{r}} \\ &= I_0\frac{\partial H(r - r_0)}{\partial r}\hat{\mathbf{r}} \\ &= I_0\delta(r - r_0)\hat{\mathbf{r}}.\end{aligned}$$

The ITE therefore becomes Poisson equation with Neumann boundary condition:

$$\begin{cases}\nabla^2\phi = -\frac{k}{I_0}\frac{\partial I}{\partial z},\ r < r_0 \\ \frac{\partial \phi}{\partial r} = -\frac{k}{I_0}\frac{\partial I}{\partial z},\ r = r_0.\end{cases} \tag{2-13}$$

While the derivation process is lengthy, the physical meaning is simple and represented in Figure 2-1. Positive curvature of the wavefront results in negative z-derivative of the intensity profile, i.e. locally divergent beam, and thus produces spot of lower intensity after propagation by positive distance z_0. Similarly, negative curvature yields positive z-derivative of intensity, and produces local bright spot.

Information about phase Laplacian inside beam footprint can therefore be obtained by measuring z-derivative of intensity distribution. Based on that, Teague [7] proposed a scheme of

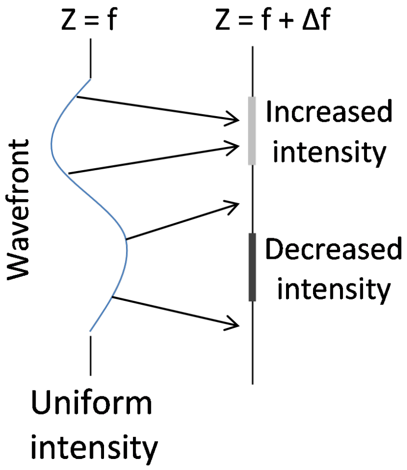

Figure 2-1: Physical interpretation of the Transport of Intensity Equation.

phase retrieval using Equation (2-13). Following the previous notation, the intensity $I(\mathbf{r}) = I_0$ is assumed to be uniform in plane $z = 0$. Phase in this plane is recovered from measurement of intensity $I(\mathbf{r})$ in plane $z = z_0$. The z-derivative of intensity distribution is approximated by measurements in two planes,

$$\frac{\partial I}{\partial z} \approx \frac{I_{z_0} - I_0}{z_0}, \tag{2-14}$$

where I_{z_0} is the intensity distribution in the plane $z = z_0$. The schema of this method is represented in Figure 2-2.

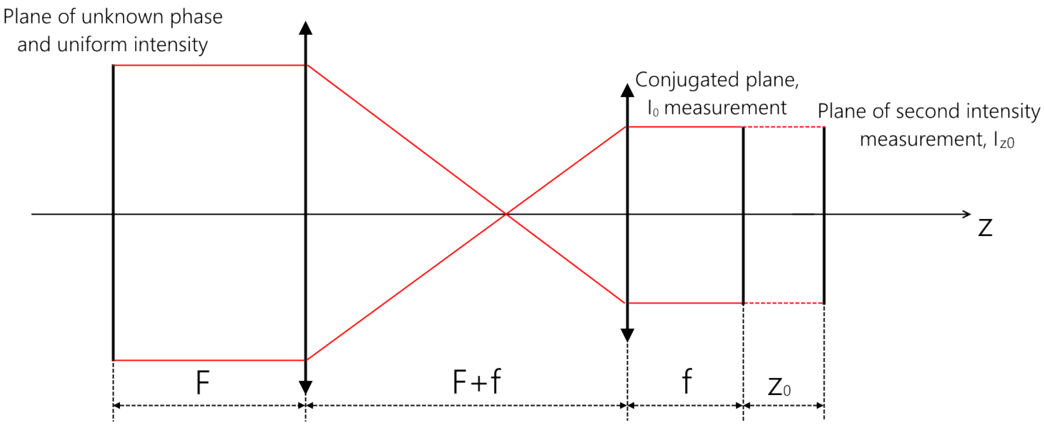

Figure 2-2: Schematic representation of the phase retrieval using ITE [7]

The intensity distributions are measured in two planes separated by the distance z_0. Plane of unknown phase is conjugated to the plane of first measurement, $z = 0$, via Keplerian telescope formed by the two lenses of focal lengths F and f, $f < F$. Here the uniform intensity I_0 is measured. The plane of second measurement I_{z_0} is separated from the first plane by distance z_0. Here the intensity distribution is modulated by unknown phase curvature. The magnification $m = \frac{f}{F}$ is needed to enhance intensity variations induced by the phase curvature for small displacement distances z_0.

Equation (2-13) is an equation based on certain approximations, which limit its region of validity, for instance Equation (2-13) does not hold near lens focal. In order to have an approximation on propagation distance over which the equation remains valid, intensity $I_{\delta z}$ in the plane $z = \delta z$ near the plane $z = 0$ is expanded as [7]

$$I_{\delta z} = I_0[1 + b_1\delta z + b_2(\delta z)^2] + \Delta I_0,$$

where

$$b_1 = -2(\frac{\lambda}{4\pi})\ \nabla^2\phi\Big|_{z=0}, \tag{2-15}$$

$$b_2 = 4(\frac{\lambda}{4\pi})^2\ [(\phi_{xx})^2 + \phi_x\phi_{xxx} + \phi_{xx}\phi_{yy} + \phi_y\phi_{yyy} + (\phi_{yy})^2]\Big|_{z=0}, \tag{2-16}$$

and ΔI_0 is the noise term. Ignoring the latter, for a given phase aberration the ITE is valid if

$$b_2\delta z \ll b_1, \tag{2-17}$$

and this allows to choose δz for a known or expected phase aberration. If the incoming aberration is stochastic, but the upper boundary is known, as in case when it is created by random voltages on Deformable Mirror (DM) actuators, all terms in Equation (2-15) can be calculated for largest actuator displacement, allowing to select δz such that the sensor readings are linear during the mirror operation.

The above derivations explain how a simple curvature sensor built from two CCD cameras works. It will be used later in this thesis in combination with a DM to build closed loop adaptive optics system.

2-2 Imaging theory

As mentioned before, aberrations reduce image quality significantly. Prior to diving into Adaptive Optics, theory of image formation is explained. This knowledge helps to understand better the effect of aberrations on image quality, as well as certain notions and metrics useful for Adaptive Optics (AO). In this section basic theory of image formation is given. The notation and derivations are adapted from [5].

Assume the object is located in $x - y$ plane at distance d_o in front of the positive diffraction-limited lens with focal distance f. The object is illuminated and the object field is $U_o(\xi, \eta)$, where (ξ, η) are the coordinates in the object plane. Geometrical optics predicts image formation at distance d_i from the lens, where d_i can be calculated from the thin lens formula:

$$\frac{1}{f} = \frac{1}{d_o} + \frac{1}{d_i}. \tag{2-18}$$

The magnification M of this simple imaging system is given by

$$M = \frac{h_i}{h_o} = \frac{d_i}{d_o}, \tag{2-19}$$

where h_o and h_i are image and object heights, respectively. Assume the illumination field is coherent and let the image field be $U_i(u, v)$, where (u, v) are the coordinates in image plane. Because of the linear nature of the propagation phenomenon, the image field can be related to the object field by the following integral:

$$U_i(u, v) = \int \int U_o(\xi, \eta) h(u, v; \xi, \eta) d\xi d\eta, \tag{2-20}$$

where $h(u, v; \xi, \eta)$ is the image field amplitude produced at coordinates (u, v) in the image plane by a point disturbance at coordinates (ξ, η) in the object plane with unit amplitude, i.e. the impulse response of the imaging system. The integral can be reduced to convolution integral, and the image field becomes [5]:

$$U_i(u, v) = \int \int h(u - \tilde{\xi}, v - \tilde{\eta}) U_g(\tilde{\xi}, \tilde{\eta}) d\tilde{\xi} d\tilde{\eta}. \tag{2-21}$$

This integral expresses convolution operation, which defines image field in terms of geometrical optics prediction of the image, U_g:

$$U_i(u, v) = h(u, v) * U_g(u, v). \tag{2-22}$$

Here, $\tilde{\xi} = M\xi$, $\tilde{\eta} = M\eta$, $U_g(u, v)$ is the geometrical optics prediction of the image,

$$U_g(u, v) = \frac{1}{|M|} U_o\left(\frac{u}{M}, \frac{v}{M}\right), \tag{2-23}$$

and $h(u, v)$ is the Point Spread Function (PSF) of the imaging system:

$$h(u, v) = \int \int P(x, y) e^{-i \frac{2\pi}{\lambda d_i}(ux + vy)} dx dy. \tag{2-24}$$

The PSF of an optical system is the image field distribution when the object is point disturbance. From Equation (2-24) it follows that the PSF of a system is the Fourier transform of the (complex) transmittance function $P(x, y)$ of the exit pupil, also called pupil function, evaluated at spatial frequencies

$$f_x = \frac{u}{\lambda d_i},\ f_y = \frac{v}{\lambda d_i},$$

i.e. the Fraunhoffer diffraction pattern of the exit pupil. Thus it has been shown that the image is obtained as the result of convolution of the image predicted by geometrical optics, which is infinitely sharp scaled object, convolved with the PSF of the imaging system. The effect of the convolution is to smoothen the image, and kernel is PSF of the imaging system used. For a system which consists of one lens with radius R_{lens} and focal F the pupil function is given by

$$P(x, y) = \mathrm{circ}\left(\frac{\sqrt{x^2 + y^2}}{R_{lens}}\right),$$

such that $P(x, y) = 1$ for (x, y) inside the aperture and $P(x, y) = 0$ for (x, y) outside the aperture. The PSF in this case is given by

$$I(u, v) = I_0 \frac{\pi^2 R_{lens}^4}{F^2 \lambda^2} \left(\frac{2J_1(\rho)}{\rho}\right), \tag{2-25}$$

where I_0 is incident field intensity, λ is wavelength of illumination, $J_1(\rho)$ is Bessel function of the first order, and ρ is given by

$$\rho = \frac{2\pi R_{lens}}{F\lambda} \sqrt{u^2 + v^2}. \tag{2-26}$$

The width w of this PSF is given by the position of first minimum of the Bessel function:

$$w = 0.61 \frac{\lambda}{NA}, \tag{2-27}$$

where $NA = \frac{R_{lens}}{F}$ is the numerical aperture. This defines the Rayleigh resolution for a diffraction limited system, the fundamental upper limit on resolution of a usual imaging system: in far field two points of an object are resolved if the PSFs produced by these points are separated by w.

In case of incoherent imaging, the same relations hold for intensities of the object and image fields:

$$I_i(u,v) = h_{inc}(u,v) * I_g(u,v), \tag{2-28}$$

where h_{inc} is the incoherent PSF of the system, and $I_i(u,v)$ is the image intensity, $I_i(u,v) = |U_i(u,v)|^2$. The relation between incoherent and coherent PSF is

$$h_{inc} = |h_{coh}|^2. \tag{2-29}$$

In the framework of Fourier optics, the image is smoothened, scaled and rotated version of the object field. A system, where the point source at the input yields a perfect spherical wavefront converging to the ideal geometrical image point, is called diffraction limited. For such systems the transmittance function is purely real, or complex with constant phase factor, and the resulting PSF is narrow and bright. Aberrations in general result in wider and darker PSFs. An example of effect of aberrations on incoherent imaging is represented in Figure 2-3.

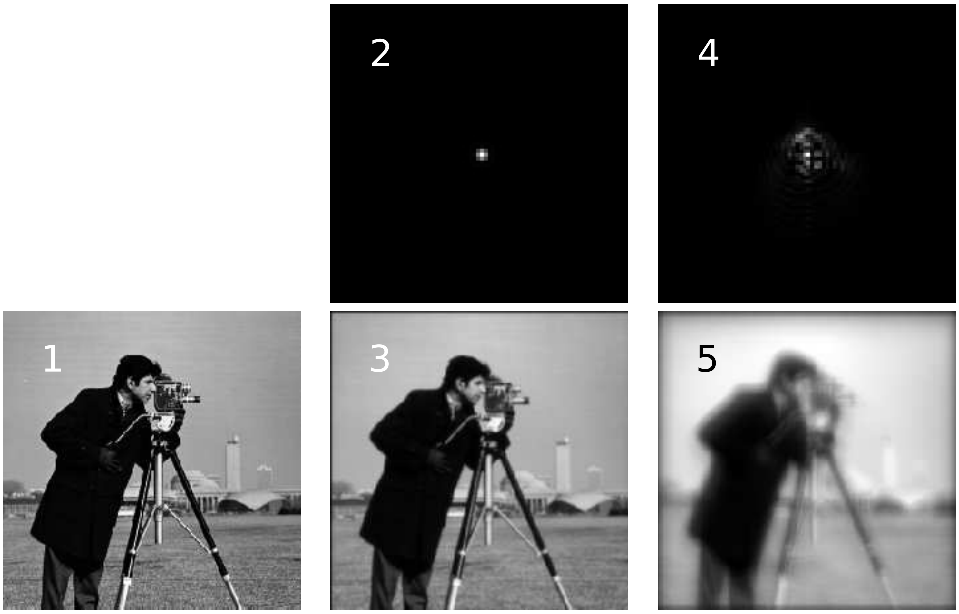

Figure 2-3: Example effect of aberrations on image formation. The imaged object is represented in (1). The diffraction-limited PSF of the simulated system is represented in (2), and the diffraction-limited image is represented in (3). The PSF of the system with aberrations present is represented in (4), and the image formed in this condition is in (5).

The imaged object is represented Figure 2-3, (1). The simulated optical system is a simple lens. In the diffraction-limited case, the pupil function is

$$P(x,y) = \text{circ}\left(\frac{\sqrt{x^2+y^2}}{R_{lens}}\right),$$

s.t. $P(x,y) = 1$ for (x,y) inside the aperture, and $P(x,y) = 0$ for (x,y) outside the aperture. The PSF of the simulated system is represented in Figure 2-3 (2), and the resulting diffraction-limited image is in (3). The aberrated PSF (4) is clearly wider than in the diffraction-limited case, and results into blurred aberrated image (5), and a lot of details are lost. One of the several possible ways to quantify the quality of an imaging system is Strehl ratio, defined as the ratio of maximal intensities of aberrated and diffraction limited PSFs:

$$S = \frac{I_{ab,max}}{I_{dl,max}}. \tag{2-30}$$

Strehl ratio is related to RMS value σ or variance σ^2 of phase. For relatively small aberrations with $\sigma \lessapprox 2\,\mathrm{rad}$, Strehl ratio can be calculated by Marechal approximation:

$$S = e^{-\sigma^2}, \tag{2-31}$$

where σ is wavefront RMS value in radians. For an ideal diffraction limited optical system $S = 1$, and in general $S \in (0, 1]$. Later in this work $S = 0.8$ is considered to provide good image quality.

In this section it was explained how aberrations affect image quality. One usually wants to resolve the smallest possible details of the object of interest, and therefore the incoming wavefront must be as flat as possible, which is equivalent of maximizing Strehl ratio of the imaging system. Wavefront aberrations contribute partly from the imaging system itself, and this contribution can be compensated easily. However, a significant effect comes from external aberrations depending on media between the resolved object and imaging system, and cannot be accounted for by simply improving optics quality. Adaptive Optics (AO) provides solution to this problem and allows to compensate for changing external aberrations and improve the image quality.

2-3 Adaptive Optics

Adaptive Optics (AO) is a set of techniques that allow to correct static and dynamic wavefront aberrations and improve image quality. In this section basic structure and principles of AO optical system are explained, namely general structure of AO loop, a basis for aberration reconstruction called Zernike polynomials, basic principles of operation of membrane Deformable Mirror (DM) and its relevance to the subject, Shack-Hartmann (SH) Wavefront Sensor (WFS), and finally the Curvature Sensor (CS).

2-3-1 Basic principles

Adaptive Optics (AO) is a scientific and engineering discipline whereby the performance of an optical signal is improved by using information about the environment through which it passes [8]. Usually the adaptive optical system deals with control of light in a real-time

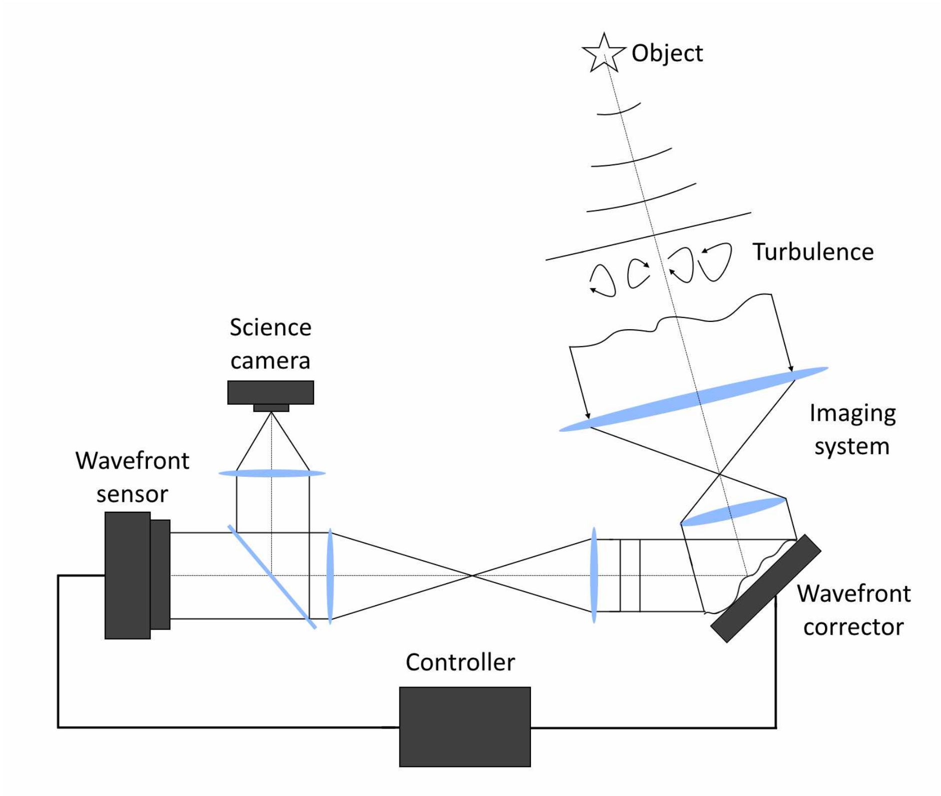

Figure 2-4: A basic structure of AO loop. The aberrated wavefront is incident onto the imaging system. The deformable mirror in the exit pupil of the imaging system is driven by a controller and applies the correction such that the reflected wavefront is as flat as possible. The residual aberration of the wavefront is measured by a wavefront sensor. The image of the object is formed at the science camera.

closed-loop fashion. A basic structure of astronomical adaptive optics loop is represented in Figure 2-4.

The object located at infinity emits light. Before passing through turbulent layers of air, the wavefront can be considered flat. Turbulence induces aberrations $\phi(\mathbf{r}, t)$ to the wavefront incident onto imaging system (telescope in this case) [9]. The Deformable Mirror (DM), located in the plane conjugated to turbulence layer, applies the phase correction $\phi_c(\mathbf{r}, t)$ by changing profile of its surface, and upon reflection from the DM [10] the wavefront phase is $\epsilon = \phi - \phi_c$. The residual wavefront phase is often assumed to be zero-mean signal, since constant phase offset across the aperture is of no physical significance and does not affect image quality. Input voltages to the DM are calculated on-line by control algorithm based on data provided by Wavefront Sensor (WFS), such that $\epsilon \to 0$. Since detectors are able to measure only the intensity $I(x, y) = UU^*$, where U is the complex field amplitude, the phase cannot be measured directly. Therefore, the WFS does not measure the residual aberration $\epsilon = \phi - \phi_c$, but some other function of the residual phase, for instance first derivative or Laplacian. WFS is usually assumed to be a linear system, therefore the output signal is modeled as $\mathbf{s} = G\epsilon + \eta$, where G is determined by the sensor type and geometry and η is additive noise. The measurement is input to the controller, and the output is the actuator signals $\mathbf{u}$ applied to the deformable mirror such that the variance of residual aberration

$\sigma^2 = \epsilon^T\epsilon$ is minimized. The image is finally formed at science camera.

It is often useful to expand a function defined over 2-D circular pupil as a weighted sum of certain basis functions. There is an infinite number of possible basis, but in AO the most widely used is basis of Zernike polynomials, discussed in the next section.

2-3-2 Zernike Polynomials

Within the framework of Adaptive Optics, the phase inside a circular aperture is usually decomposed into the basis of Zernike polynomials [11], defined as

$$Z_n^m = \sqrt{n+1}R_n^m(\rho)\begin{cases}\sqrt{2}\cos(m\phi), & m>0,\\ \sqrt{2}\sin(m\phi), & m<0,\\ 1, \quad m=0\end{cases} \tag{2-32}$$

$$R_n^m(\rho) = \sum_{k=0}^{\frac{n-m}{2}} \frac{(-1)^k(n-k)!}{k!(\frac{n+m}{2}-k)!(\frac{n-m}{2}-k)!}\rho^{n-2k}, \tag{2-33}$$

where $n \in \mathbb{Z}_{\geq 0}, m \in \mathbb{Z}$, $m \leq n$, $n-m =$ even, and (ρ, ϕ) are normalized polar coordinates inside aperture, $\rho \leq 1$. The first few Zernike polynomials are represented in Figure 2-5.

Zernike polynomials present orthogonal basis over a unit circle of unit radius:

$$\frac{1}{\pi}\int d^2r Z_n^m(\mathbf{r})Z_{n'}^{m'}(\mathbf{r}) = \delta_{n,n'}\delta_{m,m'},$$

where $\delta_{i,j}$ is Kronecker symbol, $\delta_{i,j} = 1$ if $i = j$ and $\delta_{i,j} = 0$ otherwise. Given a wavefront phase $\phi(\mathbf{r})$ defined over unit circle, it can be represented as

$$\phi(\mathbf{r}) = \sum_j a_j Z_j(\mathbf{r}),$$

where j is just some ordering number used for convenience of representation. Expansion coefficients are given by

$$a_j = \frac{1}{\pi}\int d^2r Z_j(\mathbf{r})\phi(\mathbf{r}),$$

where the sum is over infinite number of coefficients in general. This way, wavefront can be represented in two equivalent ways: defining phase across the whole aperture or specifying expansion coefficients of Zernike polynomials.

Several ways to label Zernike polynomials exist. Noll's sequential indexing is also further used in this thesis [11].

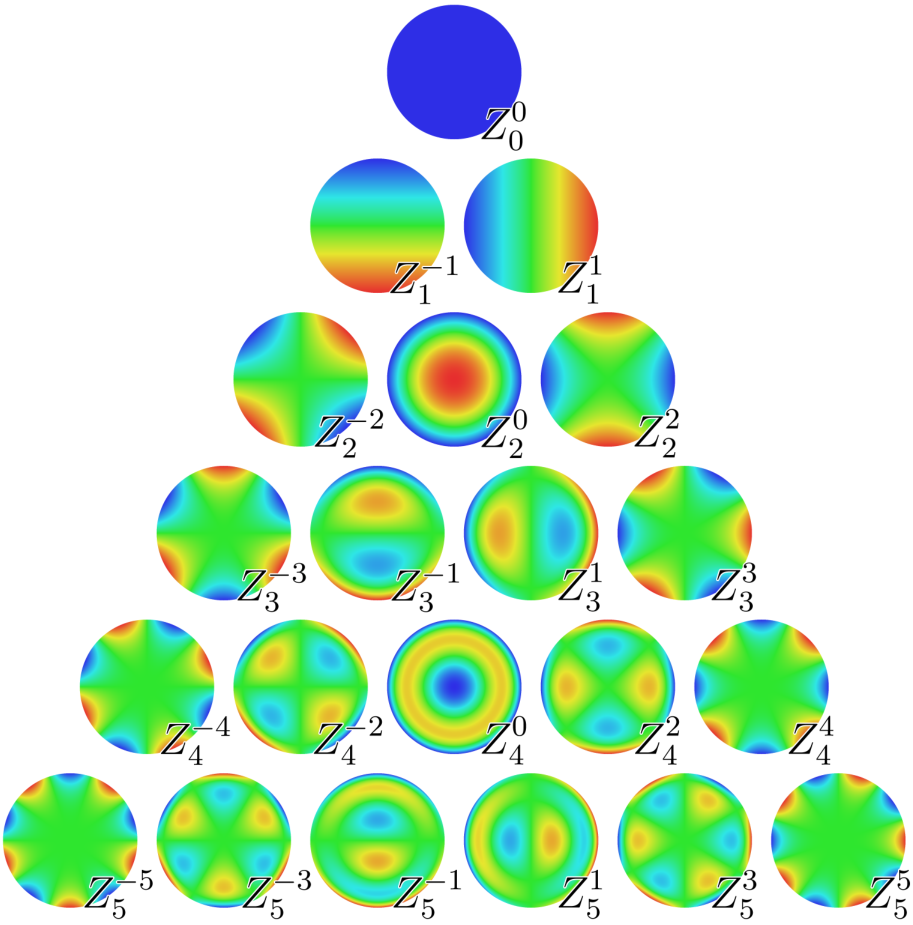

Figure 2-5: Zernike polynomials up to order $n = 5$

2-3-3 Curvature mirrors

An important element of AO loop is wavefront corrector, since it defines the best achievable correction quality. It can be either Deformable Mirror, or Spatial Light Modulator (SLM). In this thesis only a Deformable Mirror is used. Physically, a DM is a reflective surface with shape changed by actuators. The DM deformation resulting from action of each actuator separately defines mirror response functions. The type of the surface, edge actuation and clamping mode and actuator type affect the exact shape of response functions. Mathematically speaking, a DM is a device that provides a set of usually non-orthogonal basis functions in which the residual wavefront phase is decomposed.

The principles of phase curvature sensing were introduced in Section 2-1-2. Curvature mirrors are able to change local curvature of the reflecting surface, as the name suggests, and therefore can be efficiently used with Curvature Sensor (CS). An example of curvature mirror is membrane mirror ([12], [13]), which is used in experimental validation of the studied correction method. It is therefore useful to understand the basic physical principles of how the surface deforms in response to actuation, since the results are used to simulate the device.

A membrane mirror consists of a reflective membrane located between a continuous transpar-

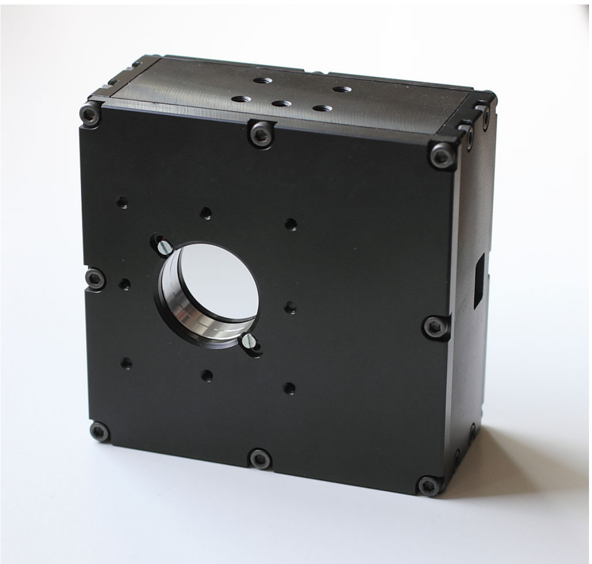

Figure 2-6: Micromachined membrane deformable mirror produced by OKOtech

ent electrode and a grid of individual electrodes. The reflective surface is deformed by means of electrostatic interaction between the electrodes and the membrane. The mirror profile $z(x, y)$ in equilibrium is the solution to Poisson equation [12],

$$\nabla^2 z(x, y) = -\frac{P(x, y)}{T}, \tag{2-34}$$

where $P(x, y)$ is the pressure due to the electrostatic interaction, and T is tension in the membrane. Given a known electrode shape, Equation (2-34) can be solved with electrostatic pressure constant across the electrode area, and the solution is then normalized to mirror actuator stroke, which is a known parameter. The wavefront phase profile induced by the mirror is given by:

$$\phi_{DM}(x, y) = 2\frac{2\pi}{\lambda} z(x, y), \tag{2-35}$$

where λ is the wavelength of light, $z(x, y)$ is the mirror surface profile, and the factor of 2 in front is because upon reflection light passes the same path twice. Assume a membrane configuration $z(x, y)$ in which all actuators are at 0 V, $u_i = 0 \, \forall i \neq n$, except for n^{th} actuator which is active, $u_n \neq 0$. Due to the nature of electrostatic interaction, the resulting pressure distribution $P(x, y)$ will be nonzero only across the surface on n^{th} actuator, and thus both $\nabla^2 z(x, y)$ and $\nabla^2 \phi_{DM}(x, y)$ are negligibly small away from the actuator surface. This means that curvature of the membrane and the induced wavefront is localized to the surface of active actuator. The same does not hold for the first derivatives of the mirror influence function. This convenient property of the Laplacian of the DM response allows for efficient coupling with CS, as it is demonstrated further.

2-3-4 Shack-Hartmann Wavefront Sensor

In a typical AO system information about the wavefront after reflection from the DM is obtained using a Wavefront Sensor (WFS). One of the most commonly used WFS, the Shack-Hartmann (SH) WFS [14], is used to measure first derivative in x and y-directions. It consists of a 2-dimensional array of microlenses of the same focal length and a detector, usually CCD camera or a quad-cell. The operating principle is represented in Figure 2-7.

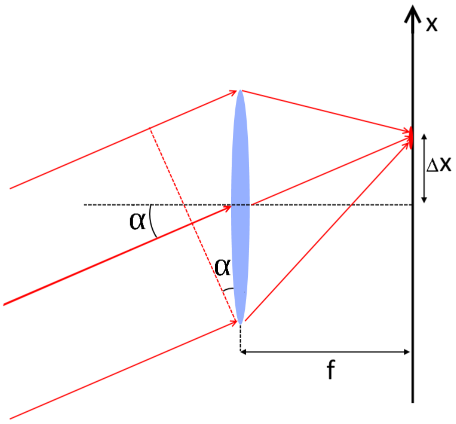

Figure 2-7: A simple single-lens system: tilted incoming beam results in focal spot, displaced in plane orthogonal to optical axis.

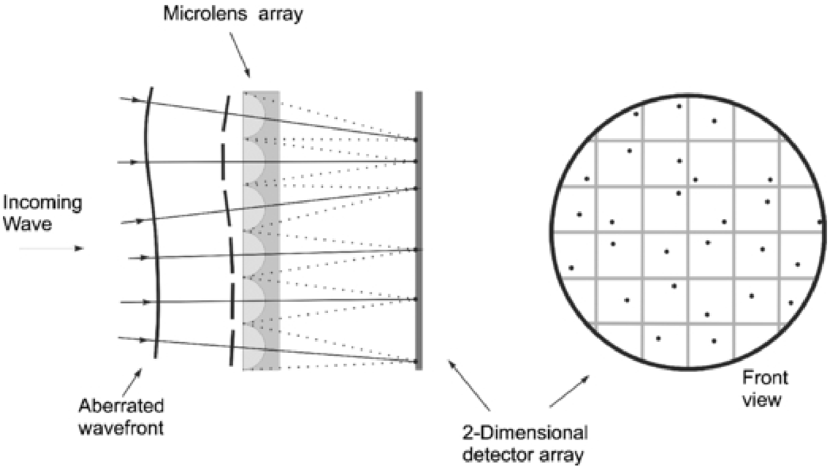

Figure 2-8: Operating principle of the Shack-Hartmann wavefront sensor. Two-dimensional array of microlenses focuses incoming light into a grid a focal spots. Displacements of the foci from a reference position provides information about average tilt of the incoming wavefront across corresponding microlens. Figure adapted from [15]

Wavefront across each microlens aperture is approximated by a plane wave traveling at certain angles with respect to x and y axis. Consider a 1-D case represented in Figure 2-7. An incident wavefront with zero slope forms focal spot in the focal plane of the microlens at the optical axis. An incident wavefront which makes angle α with the x-axis results in the focal spot centered around $\Delta x = f\alpha$ in the small angle approximation. The local wavefront tilt angle is given by $\alpha = \frac{\partial W}{\partial x}$, or $\alpha = \frac{2\pi}{\lambda}\frac{\partial \phi}{\partial x}$. Therefore, the focal spot displacement from the reference position is related to the local first derivative of the wavefront:

$$\frac{\partial\phi}{\partial x} = \frac{\lambda}{2\pi}\frac{\Delta x}{f}.$$

A Shack-Hartmann wavefront sensor consists of a 2-D array of such microlenses (Figure 2-8), therefore it measures local first x and y derivatives sampled at the positions of the microlenses. The focal spot displacements (x_i, y_i) are calculated by the centroid algorithm as the center of mass position of the intensity distribution in the detector plane:

$$\Delta x_i = \frac{\sum_{x,y} xI(x,y)}{\sum_{x,y} I(x,y)},$$
$$\Delta y_i = \frac{\sum_{x,y} yI(x,y)}{\sum_{x,y} I(x,y)}.$$

A Shack-Hartmann wavefront sensor outputs the vector of centroid displacements in each subaperture:

$$s_x(i,j) = f\frac{2\pi}{\lambda}\frac{\partial\phi(x_i,y_j)}{\partial x} + \eta_x(i,j),$$
$$s_y(i,j) = f\frac{2\pi}{\lambda}\frac{\partial\phi(x_i,y_j)}{\partial y} + \eta_y(i,j),$$

where η_x, η_y are additive noise terms. To summarize, Shack-Hartmann Wavefront Sensor measures gradient of incident wavefront sampled at the positions of its microlenses. The output is displacement of the measured focal spot center of mass with respect to some reference position.

In adaptive optics with SH WFS the vector of centroid displacements $\mathbf{s}$ is assumed to be linearly related to the vector of linearized inputs of the deformable mirror actuators, $\mathbf{u}$, through the influence matrix H:

$$\mathbf{s} = H\mathbf{u}. \tag{2-36}$$

In order to close the loop, influence matrix H needs to be measured, so one needs to understand what are the entries of H. Assume the input vector $\mathbf{u} \in \mathbb{R}_N$, where N is the total number of actuators, takes the form $u_i = 0\,\forall i \neq n$, $u_n = 1$. Equation (2-36) takes the form

$$\mathbf{s} = \begin{bmatrix}\mathbf{h}_1 & \mathbf{h}_2 & \dots & \mathbf{h}_\mathbf{N}\end{bmatrix}\mathbf{u} \tag{2-37}$$
$$= \mathbf{h}_n, \tag{2-38}$$

where $\mathbf{h}_i$ are the columns of the influence matrix H. But on the left of Equation (2-37) there is vector of centroid displacements measured with n^{th} actuator signal set to 1. It becomes evident that columns of the influence matrix contain vectors of centroid displacements in response to corresponding actuator set to $u_i = 1$. This model discards the dynamic response of the deformable mirror, but for the purpose of this thesis the model is accurate enough, and it is commonly used in AO.

By performing adaptive optics correction of the wavefront, the algorithm attempts to best approximate the wavefront aberration $\phi(x, y)$ with a linear combination of influence functions of the corrector, $\phi_{DM}(x, y)$. This problem can be formulated in least squares formalism [16]. Given the vector of SH measurements with aberrated incoming beam, $\mathbf{s}$, the set of basis vectors as columns of the intensity matrix H, and the unknown vector of coefficients $\mathbf{u}$ (actuator voltages), the model is

$$\mathbf{s} = H\mathbf{u} + \epsilon,$$

where ϵ is the fitting residual. The goal is to minimize the variance of ϵ, $\text{var}(\epsilon) = \epsilon^T\epsilon$, and the problem reads as

$$\begin{aligned} &\min_{\mathbf{u}} \epsilon^{\mathbf{T}}\epsilon, \\ &\text{s.t. } \epsilon = \mathbf{s} - H\mathbf{u}. \end{aligned}$$

The solution to this least squares problem is given by

$$\hat{\mathbf{u}} = H^{\dagger}\mathbf{s},$$

where $H^{\dagger} = (H^T H)^{-1} H^T$ is the pseudo-inverse of the influence matrix H. If the matrix $H^T H$ is invertible, then the solution is readily obtained. Given incoming aberrated wavefront and corresponding SH measurement $\mathbf{s}$, the set of actuator voltages given by $\mathbf{u} = (H^T H)^{-1} H^T \mathbf{s}$ is the best approximation of the incident wavefront with the mirror influence functions.

In practice, the matrix $H^T H$ often has singularities, and is thus not invertible. In this case, the pseudo-inverse of the influence matrix is calculated using Singular Value Decomposition (SVD) [16]. For a $m \times n$ matrix H, $m > n$, the SVD of H is defined as

$$H = USV^T,$$

where S is $m \times n$ matrix of ordered singular values, $\sigma_1 > \sigma_2 > ... > \sigma_n$, with the singular values along its main diagonal, U and V^T are orthonormal $m \times m$ and $n \times n$ matrices containing left and right singular vectors respectively. In the absence of noise in case of singular matrices of rank $r < m$, $r < n$, the smallest singular values $\sigma_r \ldots \sigma_n = 0$. However for the matrices derived from noisy data this will not be the case, and these singular values will have some small but nonzero value. The pseudo-inverse of the influence matrix is then defined as

$$H^\dagger = VS^{-1}U^T,$$

where the matrix S^{-1} has the terms $\sigma_1^{-1} \dots \sigma_r^{-1}$ along the main diagonal, and zeros everywhere else. The choice of number of singular values r to include in the inversion is somewhat arbitrary, and can be made based on the desired condition number.

Given AO closed loop with SH sensor and a DM with N actuators, the smallest number of microlenses required to reconstruct actuator inputs $\mathbf{u}$ is $N_{min} = \frac{N}{2}$, since each microlens provides two measurement, one along each axis. In real systems this number usually is increased to $N_{min} \geq N$ to avoid singularities. With recent technological advances in micromachining there is a trend to increase number of DM actuators to get as close as possible to diffraction limit. Increased actuator number N poses several challenges to SH-based AO systems, such as the necessity to increase microlens density, and the computational burden, which scales as N^2 for a typical SH influence matrix. A Curvature Sensor avoids these particular issues, and is presented in the next section.

2-3-5 Curvature sensor

Shack-Hartmann wavefront sensor is based on measuring the first derivative of the wavefronts. As explained in Section 2-1-2, it is also possible to measure Laplacian of the phase, $\nabla^2\phi(x,y)$, by measuring the z-derivative of intensity distribution. Curvature Sensor (CS) is based exactly on this principle. Recall Intensity Transport equation Equation (2-13) inside the beam footprint of radius r_0:

$$\nabla^2\phi = -\frac{k}{I_0}\frac{I_{z_0} - I_0}{z_0}, \; r < r_0, \tag{2-39}$$

where z-derivative of intensity distribution is approximated as finite difference of two measurements. Roddier proposed [17] to close the Adaptive Optics loop based on the measurement of z-derivative of intensity. Since Laplacian is a linear operator, the measurement is expected to be linear with respect to control signals. The method is of particular interest when applied in combination with deformable mirrors capable of adjusting their curvature. By comparing Equation (2-39) and Equation (2-34) the relation between the pressure distribution $P(x,y)$ and approximated z-derivative of intensity becomes evident:

$$P(x,y) \propto \frac{I_{z_0} - I_0}{I_0}. \tag{2-40}$$

The quantity $\frac{I_{z_0}-I_0}{I_0}$ is further referred to as the intensity distribution. Since, as mentioned before, the pressure distribution is localized to the actuator footprint and is linear with respect to the control input $\mathbf{u}$, the control signals can be reconstructed from the local intensity signal withing the corresponding actuator surface. This leads to the influence matrix with dominant diagonal terms and small condition number [18]. Thus applying control signal proportional to local intensity distribution corrects local curvature.

In his paper, Roddier proposed to use two defocused images of pupil to obtain the curvature information. The setup is represented in Figure 2-9.

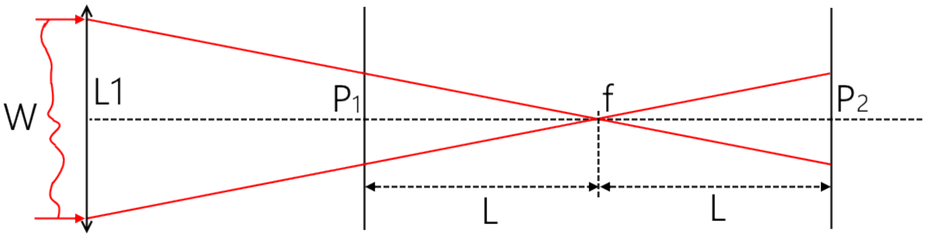

Figure 2-9: Roddier curvature sensing principle: incoming wavefront W with surface profile $z(x, y)$ is imaged in two planes, P_1 and P_2. The curvature information is reconstructed from the difference of the two images.

The incoming wavefront W with surface profile $z(x, y)$ is focused by the lens L_1 with focal length f. The two planes of intensity measurements, P_1 and P_2 are located symmetrically at distance L with respect to focal point f. In this way, the proposed method is insensitive to non-uniformities of illumination pattern.

In order to obtain the boundary condition for Equation (2-13) Roddier proposes to use intensity information at the boundary of the aperture. In principle radial tilts indeed produce variations in intensity at the beam boundary, however the signal is produced in narrow region where diffraction from the aperture boundary is significant, and is hard to be used in experimental environment. A possible way is to perform curvature correction inside beam footprint only. However, this method leaves Zernike modes Z_n^m with $\pm m = n$ uncorrected ([19], [20]):

$$\nabla^2 Z_n^{\pm n} = 0.$$

In particular this means that closed loop system based only on curvature sensing inside the beam footprint is not capable of correcting astigmatism, which is typically a high magnitude mode. Therefore, an alternative way to extract correct boundary conditions is proposed further in this thesis.

Curvature-based Adaptive Optics has been developed and used extensively in the University of Hawaii ([21], [22], [23]). Curvature-based AO has been shown [24] to yield 30 times Strehl ratio improvement with 36-channel bimorph DM at Gemini 8-meters telescope.

In this thesis the setup proposed by Teague [7] is used, since it gives exactly similar curvature information and is easier to align correctly. The schematic representation of the setup is in Figure 2-2. The setup must be correctly paired with the deformable mirror in use by choosing displacement distance between the measurement planes z_0 correctly. Physically it means that it is necessary to ensure that ITE is valid at largest actuator displacements. Recall the condition of validity of ITE is [7]:

$$b_2 z_0 \ll b_1, \tag{2-41}$$

where

$$b_1 = -2(\frac{\lambda}{4\pi})\nabla^2\phi, \tag{2-42}$$

$$b_2 = 4(\frac{\lambda}{4\pi})^2 \left[(\phi_{xx})^2 + \phi_x\phi_{xxx} + \phi_{xx}\phi_{yy} + \phi_y\phi_{yyy} + (\phi_{yy})^2\right]\Big|_{z=0}. \tag{2-43}$$

Consider a membrane deformable mirror with aperture radius a. When all actuators are active, the mirror surface has parabolic profile

$$z(x,y) = A(x^2+y^2), \tag{2-44}$$

where the proportionality constant A is defined by the total stroke of the mirror. Assume the peak-to-valley displacement of the mirror surface is $n\lambda$, where λ is the wavelength of light. When used in biased mode, membrane mirrors are capable of generating only half of this stroke. Then

$$z(x,y) = \frac{n\lambda}{2a^2}(x^2+y^2). \tag{2-45}$$

The phase induced by the mirror is

$$\phi_{DM}(x,y) = \frac{2\pi n}{a^2}(x^2+y^2). \tag{2-46}$$

For this phase aberration, the coefficients are

$$b_1 = -\frac{4\lambda n}{a^2}, \tag{2-47}$$

$$b_2 = \frac{12\lambda^2 n^2}{a^4}, \tag{2-48}$$

therefore the condition on the defocus distance reads

$$z_0 < \frac{a^2}{3n\lambda}. \tag{2-49}$$

This factor is not exactly instructive and it is possible to rewrite it. The phase profile induced by the lens with focal length f is

$$\phi_{lens}(x, y) = \frac{\pi}{\lambda f}(x^2 + y^2). \tag{2-50}$$

By comparing Equation (2-50) and Equation (2-46) it can be seen that the focal length of the mirror is

$$f_{DM} = \frac{a^2}{2\lambda n},$$

and the condition on defocus distance reads

$$z_0 < \frac{2}{3} f_{DM}. \tag{2-51}$$

When the telescopic system with magnification m is used to reimage the mirror surface, the condition becomes

$$z_0 < m^2 \frac{2}{3} f_{DM}. \tag{2-52}$$

In practice the method was observed to converge for z_0 comparable to f.

Another useful influence function to investigate is Gaussian response of the mirror surface. This corresponds to model of influence function of high-order deformable mirrors with circular aperture, where the surface is thin metal plate. Taranenko [25] found the influence functions of copper and aluminum plates closely follow either Gaussian or super-Gaussian response. Let the actuator influence function be

$$z(x, y) = Ae^{-\frac{x^2+y^2}{2\sigma^2}}, \tag{2-53}$$

where parameter A is related to actuator stroke, and standard deviation σ is related to interactuator influence function overlap. If d is the interactuator distance, and γ is the overlap coefficient, meaning that influence function has $\gamma \times$ stroke at distance d, the standard deviation is

$$\sigma = \sqrt{\frac{d^2}{2 \ln \gamma^{-1}}}. \tag{2-54}$$

The calculations for Gaussian yield

$$z_0 < \frac{2\sigma^2}{3A} \tag{2-55}$$

$$< \frac{d^2}{3A \ln \gamma - 1}, \tag{2-56}$$

and if the magnification m is used to image the surface of the mirror, the upper boundary on z_0 becomes

$$z_0 < \frac{m^2 d^2}{3A \ln \gamma^{-}1}. \tag{2-57}$$

The upper bound on the defocus distance z_0 defines the applicability of the method. The quantity that is measured in plane $z = z_0$ is

$$I_{z_0} - I_0 = -z_0 k I_0 \nabla^2 \phi + \eta, \tag{2-58}$$

where η is the noise term. Noise can be described as the sum of two terms, one dependent and one independent on I_0. Therefore if I_0 is small, which is condition of low illumination, $I_{z_0} - I_0$ is also small and the signal to noise ratio is decreased. In order to increase it back, z_0 must be increased, but only up to the upper limit after which the ITE does not hold anymore.

To summarize, Curvature Sensor is expected to have the following features:

1. Curvature signal generated by the curvature mirrors is mostly confined to the area of corresponding actuator. This results in nearly diagonal influence matrix and greatly reduces computational costs.
2. Since linearized actuator input signal is directly proportional to produced curvature and local increase of intensity, analog high-speed feedback loop with photon counting avalanche photo diodes can be used [21].
3. Since in this case the phase curvature is essentially sampled by each pixel and not by each microlens subaperture as in SH case, sampling is much more dense and therefore the sensor is expected to be less affected by aliasing than SH.

4. Assume phase $\phi(\mathbf{r})$ is given by a single-frequency sinusoid:

   $$\phi(\mathbf{r}) = \sin(\mathbf{k} \cdot \mathbf{r}).$$

   Its gradient and Laplacian is given by:

   $$\begin{aligned} \nabla\phi &= \mathbf{k}\cos(\mathbf{k} \cdot \mathbf{r}), \\ \nabla^2\phi &= -|k|^2 \sin(\mathbf{k} \cdot \mathbf{r}). \end{aligned}$$

   Since $\nabla\phi \propto |k|$ and $\nabla^2\phi \propto |k|^2$, for hight spatial frequency components of phase $\nabla^2\phi \gg \nabla\phi$ holds. It is therefore easier to work with Laplacian instead of gradients high-order phase aberrations, where large spatial frequencies prevail.

5. Since CS is essentially two CCD cameras separated by a variable distance, it is easily tunable to different seeing conditions and expected aberrations by simply changing the separation distance. For instance, if expected wavefront is almost flat, large distance can be selected to sense the remaining small aberration. On contrary if a large aberrations are expected in the system, displacement between the cameras should be decreased to maintain validity of ITE. This parameter can as well be tuned in closed-loop during operation of the AO system: at initialization uncorrected wavefront hits the CS and Δz must be small, whereas in the middle of operation every $k+1$-st wavefront has a small deviation from k-th wavefront, and since only this residual is observed by CS, Δz can be increased to increase sensitivity. This idea is not addressed in this thesis.

This concludes the chapter with theoretical background and introduction to Adaptive Optics and Curvature Sensor. With this information it is easy to understand the contents of the next chapter, which are simulation and experimental details and results.

Chapter 3

Experiments

Roddier proposed curvature sensing method, which can be efficiently used with curvature mirrors. In his original paper he described the way to extract signal for the actuators on the beam footprint boundary purely from intensity measurements. A problem exists with this method and is addressed in this chapter. An alternative way of combining Shack-Hartmann (SH) and Curvature Sensor (CS) is proposed and evaluated in both custom-made simulation environment and experimental setup. Finally, CS is used to close the loop using high-order Boston Micromachines Kilo-DM with 952 actuators.

3-1 Correction method using intensity information only

The principle of CS explained in Section 2-3-5 is to measure beam intensity profile in two planes separated by a certain distance z_0 and to manipulate the measurements to yield distribution of Laplacian of phase, $\nabla^2\phi$, according to Equation (2-13). The physical structure of the sensor is different from the one used by Roddier. Instead, Teague's setup [7] is used, since it is easier to implement in experimental setup. The configuration is represented in Figure 3-1.

Plane P_0' is the location of the deformable mirror surface. Plane P_0 is where measurement of constant intensity I_0 is taken, and plane P_1 located at distance z_0 from plane P_0 is where I_{z_0} is measured, the modulated intensity profile. As mentioned before, the idea is to reconstruct input signal for every actuator from the measurement of phase Laplacian only across the surface of that actuator, which effectively means a diagonal sensor-actuator influence matrix. The calibration procedure is as follows:

1. Calculate $D_0 = \frac{I_{z_0} - I_0}{I_0}$ corresponding to the reference wavefront, where I_0 is nonzero intensity in plane P_0.
2. For every i^{th} mirror actuator, set $u_i = 1$, and record $D_{i,p} = \frac{I_{z_0,i} - I_0}{I_0}$, phase curvature distribution with positive actuator input. Then, set the same actuator to $u_i = -1$ and record $D_{i,n}$, curvature distribution with negative input to the actuator.

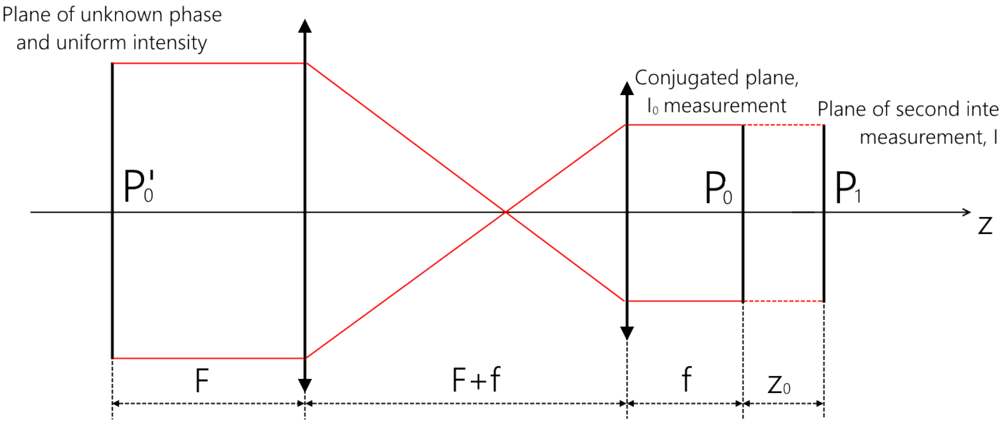

Figure 3-1: Schematic representation of the phase retrieval using ITE [7]

3. Create i^{th} actuator intensity mask M_i. Calculate $D_{i,p}-D_0$, $D_{i,n}-D_0$, take the difference and divide by 2, filter out high spacial frequencies to get rid of noise and non-uniformities but to keep the structure of actuator intensity response. Finally, set everything not in the actuator area to 0, and normalize, s.t. $\sum_{x,y} M_i \circ (D_{i,p} - D_0) = 1$, where $\circ$ denotes element-wise multiplication and the sum is over nonzero mask pixels.

For arbitrary aberration of the incident beam, the voltage reconstruction procedure is simply $u_i = \sum_{x,y} M_i \circ (D - D_0)$, where $\circ$ denotes element-wise multiplication. In other words, given a set of masks, output signal of the Curvature Sensor is calculated as the element-wise multiplication of CS image and corresponding mask, and then summation of all nonzero elements. Because of the normalization used, this also gives the voltage distribution on actuators that would generate the same aberration.

The complication in reconstruction of boundary conditions from the intensities comes from the fact that the intensity signal produced by the boundary actuators is localized to a narrow region at the edges of beam footprint, where diffraction fringes have large amplitude. Additionally, as it is shown later, the boundary actuators suffer from cross-talk. Thus the problem of reconstructing boundary conditions from intensities is experimentally complicated, and alternatives are explored.

3-2 Description of the simulations

It is beneficial to perform simulations before implementing methods in experimental setups, since all parameters and variables can be controlled in programming environments. In case of CS Adaptive Optics (AO), simulations are useful to see how the method performs with different input aberrations, a parameter that is hard to control in experiments. Finally, it is useful to make sure the method at least converges in perfect conditions, which are not achieved in experiments. For these reasons it is decided to write a simulation of studied AO system with Curvature Sensor and to perform several tests in it. All simulations are performed in a custom-written Python environment.

3-2-1 Optical Setup

Optical schematic of the simulated Curvature Sensor is represented in Figure 3-1. Incoming aberrated beam is located in plane P_0', and is conjugated to plane P_0 through Keplerian telescopic system with magnification M. In the simulation $M = 1$ is assumed. Phase and intensity of the beam in plane P_0 is assumed to be identical to ones in plane P_0'. First of all, there is no subwavelength information in the object of interest, i.e. Deformable Mirror (DM), which would be lost in the process of propagation. Under this condition, field located in the back focal plane of a lens is Fourier transform of the field in the front focal plane of the lens. Therefore from the structure of Keplerian telescope it is evident that field in plane P_0 is Fourier transform of Fourier transform of the field in plane P_0', which is just the flipped field, and flipping is insignificant for this problem. For these reasons Keplerian telescope is not simulated explicitly, instead it is assumed that DM and SH are located in plane P_0.

Amplitude and phase of the field in plane P_0 is known. Amplitude is assumed to be free parameter and is set to $|U_0| = 10$ s.t. $I_0 = 100$ in units of intensity of camera. Phase ϕ in plane P_0 is the sum of aberration phase ϕ_{ab} and phase induced by the DM ϕ_{DM}:

$$\phi = \phi_{ab} + \phi_{DM}, \tag{3-1}$$

where dependence on (x, y) position is implied. Given the field in plane P_0, it is required to simulate field in plane P_1 to complete the Curvature Sensor. Equation (3-2) is used for this purpose:

$$A(f_x, f_y, z_0) = A(f_x, f_y, 0)e^{i\sqrt{k^2-(2\pi f_x)^2-(2\pi f_y)^2}z_0}. \tag{3-2}$$

The first step is to Fourier transform the 512 × 512 pixels simulation region using Numpy Fast Fourier Transform library to obtain $A(f_x, f_y, 0)$. From the simulation grid 220 × 220 pixels correspond to 25 × 25 mm physical region, and the rest is zero padding added for proper numerical Fourier transform calculation. Second, the calculated Fourier transform is multiplied by the phase factor as in Equation (3-2), with z_0 being the propagation distance, to obtain $A(f_x, f_y, z)$. Unless specified $z_0 = 300\,\mathrm{mm}$ is used. This distance between the cameras is equal to $0.03 f_{DM}$, where f_{DM} is effective focal distance of the simulated DM at maximal defocus. Finally, to obtain field in plane P_1, inverse Fourier transform of $A(f_x, f_y, z_0)$ is taken [26].

3-2-2 Curvature Sensor

Given two fields, U_0 in plane P_0 and U_1 in plane P_1, intensity images taken by the CCD cameras are calculated to finalize simulation of Curvature Sensor. The cameras are assumed to have pixel values between 0 and 255. As mentioned before, field amplitude $|U_0| = 10$ such that intensity registered by the first camera is $I_0 = UU^* = 100$, where $\cdot^*$ denotes complex conjugation.

Real images registered by the cameras have noise added to the actual useful signal. A detailed and accurate treatment of various sources of noise in cameras is a non-trivial problem, therefore a simplified approach is chosen. White Gaussian η_w and Poisson η_p noises are added to I_0 to simulate background and shot noise [27] on the image taken by the camera:

$$I_0' = I_0 + \eta_w + \eta_p, \tag{3-3}$$

where η_w is zero-mean normally distributed random variable with variance $\sigma = 3$, $\eta_w \sim \mathcal{N}(0, 3)$ and η_p is Poisson noise from distribution

$$f(k, \lambda) = \frac{\lambda^k e^{-\lambda}}{k!} \tag{3-4}$$

with parameter $\lambda = 3.0 \frac{\text{pixel value}}{255}$ for each pixel. The parameter values were chosen such that simulation images match observed in experiment. Following the same procedure, the image I_{z_0} in plane P_1 is calculated, and the output of CS is given by $\frac{I_{z_0} - I_0}{I_0}$. An example of simulated CS output image is in Figure 3-2.

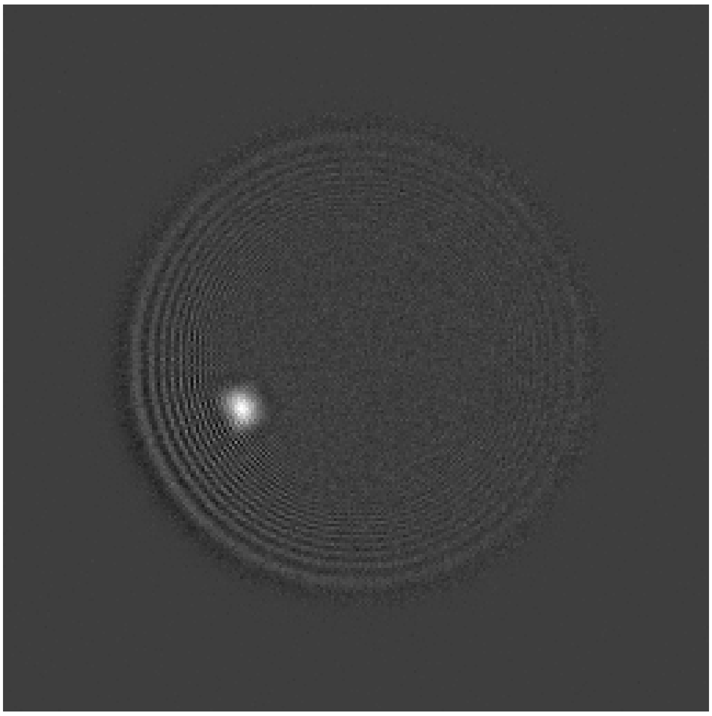

Figure 3-2: Example of simulated output of Curvature Sensor

The obtained simulation of CS is accurate enough for the goals of this thesis.

3-2-3 Deformable Mirror

An OKOtech membrane deformable mirror was modeled in simulation environment to test Curvature Sensor. The radius of DM is $r_{DM} = 110\,\text{pixels}$. For 96-channel OKO DM the actuator influence functions are calculated using iterative solver of Poisson equation,

$$\nabla^2 z(x,y) = P(x,y),$$

where $P(x,y)$ corresponds to known actuator area. Pixels corresponding to the source term on the right are inside the actuator area and are set to $+1$, and the solution pixels outside the mirror aperture are fixed to be 0. An example of calculated response for actuator 16 is represented in Figure 3-3.

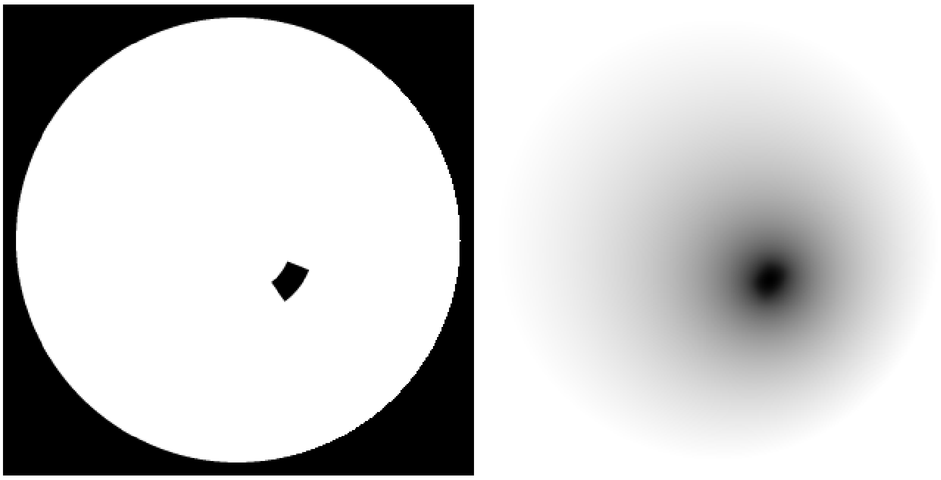

Figure 3-3: left $P(x,y)$ for actuator 16 represented inside the mirror aperture, **right** Calculated influence function

The calculated influence functions must be normalized. One can use either known single actuator stroke, or a known aberration amplitude when all actuators are active. In this case the influence functions were normalized so that upon summation they result in defocus term with 15λ amplitude at $\lambda = 550\,\mathrm{nm}$. This was done in order to sample phase appropriately on the simulation grid, i.e. at least 5 samples per 2π change of phase.

The radius of light beam is assumed to be $r_{beam} = 0.82 r_{DM} = 90$ pixels, so that its location on the mirror matches the experimental conditions.

3-2-4 Shack-Hartmann Sensor

Complete detailed simulation of Shack-Hartmann sensor can be complicated and requires simulation of propagation of light after applying a phase pattern corresponding to array of microlenses. Instead, a simpler way is chosen, since it suffices proof-of-principle goals.

Coordinates of n_{ml} microlenses are defined on a square grid inside the beam footprint. Gradient of the phase is calculated numerically and then averaged over each square microlens aperture, leaving out the unphysical jump at the boundary of aperture coming from the fact that there is no requirement that phase is zero at the boundary, but phase outside the aperture is set to 0. In this way two vectors $\mathbf{s}_x$ and $\mathbf{s}_y$ are calculated, corresponding to mean derivatives of phase in x and y directions respectively. The Shack-Hartmann output is simulated as

$$\mathbf{s} = \begin{bmatrix} \mathbf{s}_x \\ \mathbf{s}_y \end{bmatrix} + \eta,$$

where η is zero-mean white Gaussian noise. The variance is tuned such that the degree of correction approximately matches experimental observations. Two sets of lenslet coordinates are generated: for high resolution SH number of microlenses inside the beam footprint $n_{ml} = 109$ and for low resolution SH $n_{ml} = 32$. For simulations of combined SH and CS only microlenses of high-resolution SH located at the boundary are used for which $r_{ml} \geq 0.85 r_{beam}$, where r_{ml} is radial coordinate of the microlenses.

3-2-5 Atmospheric Tubulence

In order to perform tests of the proposed correction method, phase aberration with atmospheric statistics of Zernike polynomials was used. Phase screens are calculated as linear combination of Zernike polynomials with coefficients a_j being zero-mean Gaussian random variables with covariance matrix defined by Noll [11] and [28]:

$$\left\langle a_j a'_j \right\rangle = \begin{cases} 2.2698 \left(\frac{D}{r_0}\right)^{\frac{5}{3}} (-1)^{\frac{n+n'-m-m'}{2}} \sqrt{(n+1)(n'+1)} \times \\ \quad \times \frac{\Gamma([n+n'-\frac{5}{3}]/2)}{\Gamma([n-n'+\frac{17}{3}]/2)\Gamma([n'-n+\frac{17}{3}]/2)\Gamma([n+n'+\frac{23}{3}]/2)}, \text{ if } m = m' \text{ and } (j-j') \text{ even}, \\ 0, \text{ otherwise.} \end{cases} \tag{3-5}$$

Here, (n, m) and (n', m') are corresponding radial and azimuthal degree of Zernike polynomial, and $\Gamma(x)$ is Gamma-function:

$$\Gamma(x) = \int_0^{+\infty} t^{x-1} e^{-t} dt. \tag{3-6}$$

The coefficient $\frac{D}{r_0}$ is the ratio between aperture diameter and Fried length and is just a scaling factor, which in simulations is set to $\frac{D}{r_0} = 15$. Since only static aberrations have been corrected in this thesis, the tip and tilt terms are of no interest and are removed from the random phase screens.

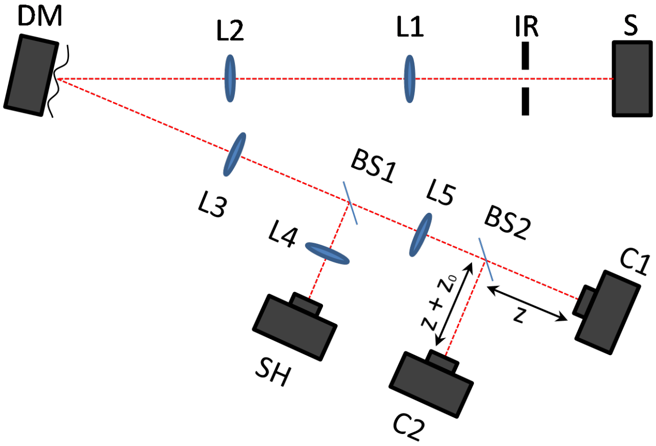

Figure 3-4: Schematic of the experimental setup.

3-3 Experimental setup

The proposed method is tested on the setup schematically represented in Figure 3-4.

The light source (S) is 472 nm LED coupled to a 50 μm multimode fiber. The iris (IR) is conjugated to the deformable mirror (DM) plane by the telescope formed by lenses L1 (100 mm focal) and L2 (300 mm focal). The magnification of the telescope system is such that the beam footprint is as represented in Figure 3-5.

The deformable mirror used in this experiment is 96-channel OKOtech membrane mirror [29]. Maximal surface retardation of the mirror is $r_{max} = 19\,\mu$m which at given wavelength is $\pm 20\lambda$ of defocus amplitude. This results in effective focal length $f_{DM} = 8.23\,$m. Since in this case the linearized signal $u \in [-1, 1]$ is used, and electrostatic membrane mirrors are able to create only convex surface, the mirror is not flat at $\mathbf{u} = 0$. The beam before the mirror must be slightly divergent so that after reflection at $\mathbf{u} = 0$ it is collimated.

The DM plane is conjugated to the Shack-Hartmann (SH) sensor through the telescope formed by the lenses L3 (300 mm focal) and L4 (100 mm focal). Microlenses with $300\,\mu$m pitch are used for SH sensor. Surface of the mirror is imaged by the two identical cameras C1 and C2 (1280×1024 ThorLabs USB camera). C1 is conjugated to the DM plane by the telescope formed by the lenses L3 (400 mm focal) and L5 (75 mm focal). In the notation used in the previous chapters, C1 measures uniform intensity distribution I_0. The second camera C2 is located at distance $z_0 = 40\,$mm from the plane conjugated to the DM, and captures the modulated intensity distribution I_{z_0}. This distance between the two CS cameras is $0.044 f_{DM}$, where f_{DM} is focal distance of the physical DM at maximal generated defocus, and it ensures that CS is operated well within the linear region.

A typical output of the curvature sensor is represented in Figure 3-6.

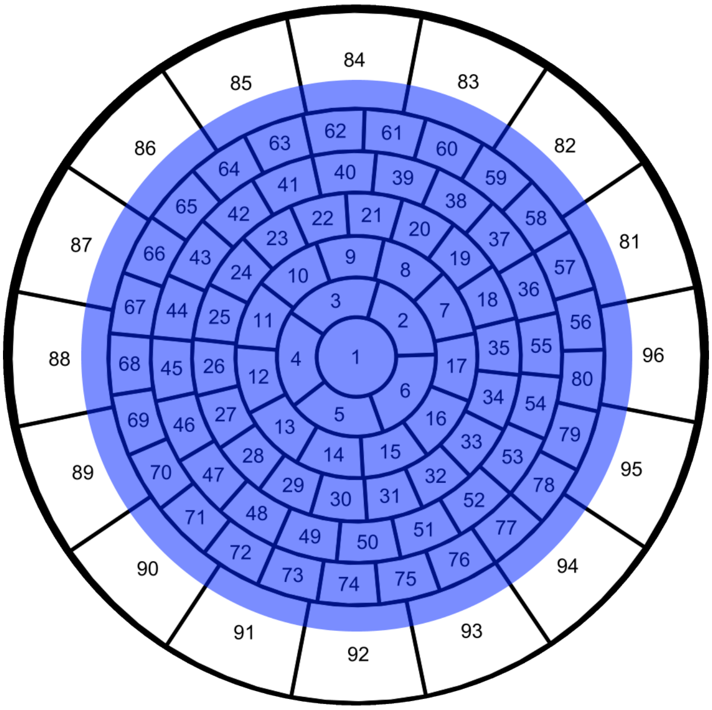

Figure 3-5: Beam geometry on the mirror.

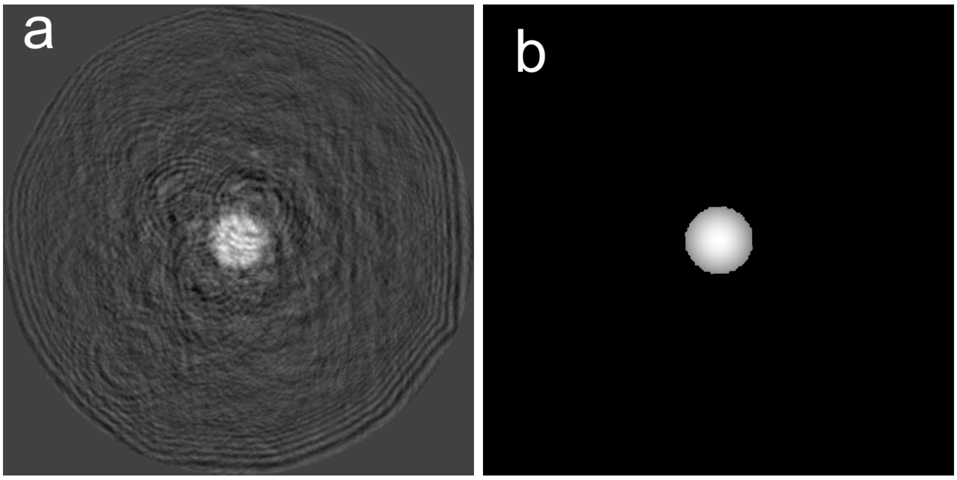

Figure 3-6: The image $D_1 - D_0$ obtained with the central actuator set to $+1$ (a) and the corresponding mask obtained from this image (b).

Figure 3-6 (a) represents $D_i - D_0$ when the input to the central actuator is $u_1 = 1$. Figure 3-6 (b) represents the mask M_1 obtained for this actuator. The selection of the part of the image corresponding to actuator surface is performed automatically, by first finding brightest pixel of filtered $D_i - D_0$, and then selecting corresponding pixels around it found from the known actuator geometry. Filtering is performed by computing Fourier transform of the image, setting pixels corresponding to spacial frequencies $|\mathbf{f}| > 10$ to 0, and computing the absolute value of inverse Fourier transform. For the boundary actuators useful signal is contained only in a narrow region at the boundary, as expected. However, it was observed that using full actuator area for the mask leads to more stable performance of AO. The signal and mask for a boundary actuator is represented in Figure 3-7.

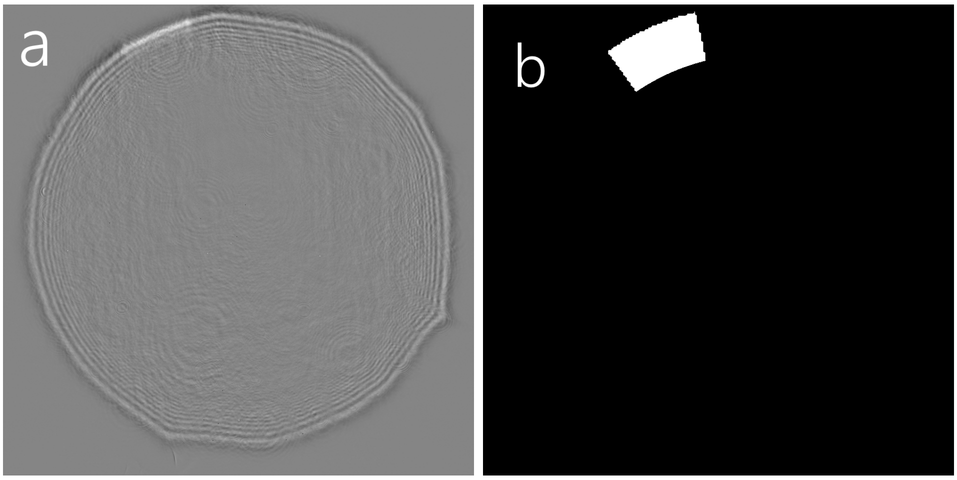

Figure 3-7: The image $D_1 - D_0$ obtained with actuator 86 set to $+1$ (a) and the corresponding mask obtained from this image (b).

3-4 Linearity of the method

The first step to be done when testing a new method is to make sure the proposed metric is indeed linear in actuator signals. For this purpose, at first a simulation is performed. Each actuator is set to range of voltages between -1 and 1, and every time the actuator voltage is reconstructed from the intensity distributions using the described method.

The mean and standard deviation of reconstructed signal plotted against the applied signal is represented in Figure 3-8 (left). The mean and standard deviation of reconstruction error is represented in Figure 3-8 (right).

It can be observed that the method indeed exhibits linear behavior, with the error due to nonlinearity not exceeding 12% of the applied voltage. Increasing the displacement distance z_0 increases the observed nonlinearity. The linearity of the reconstruction was also tested in experimental setup. The results are represented in Figure 3-9.

As it can be seen the method exhibits linear behavior in experimental setup as well, but with larger deviations. It is observed that in experiment increasing z_0 affects the linearity less than it does in the simulation. Therefore, both experiment and simulation confirm that CS output signal is linear in mirror actuator voltage, and therefore can be readily used to close the loop without extra calculations needed. In the experimental setup reconstruction error is within 20% of applied signal, which is a precision good enough for closed loop operation.

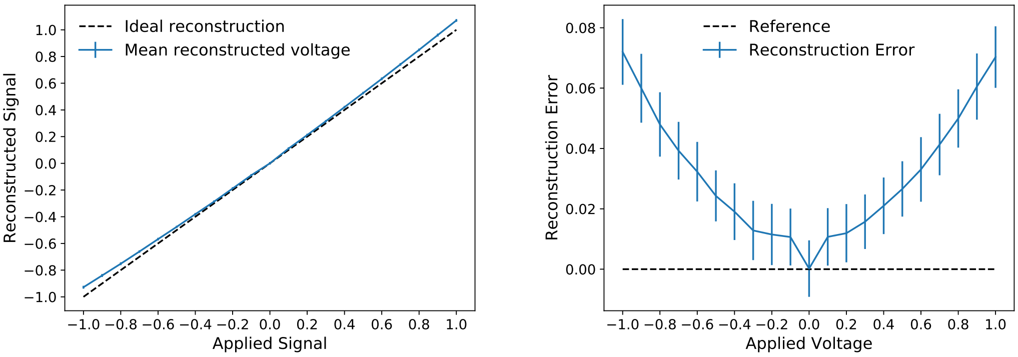

Figure 3-8: Simulation data: **(left)** Mean and standard deviation of reconstructed voltage plotted against applied voltage, **(right)** Mean and standard deviation of voltage reconstruction error plotted against applied voltage

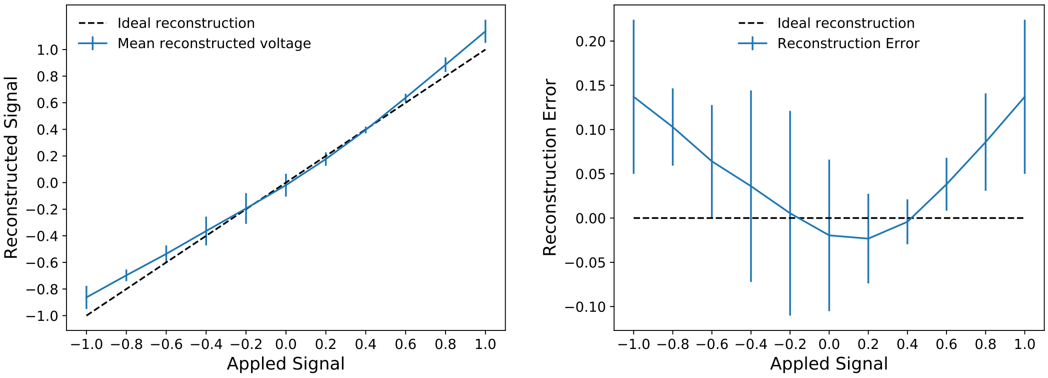

Figure 3-9: Experimental data: **(left)** Mean and standard deviation of reconstructed voltage plotted against applied voltage, **(right)** Mean and standard deviation of voltage reconstruction error plotted against applied voltage

3-5 Influence matrix obtained with membrane mirror and curvature sensor

As mentioned before, one of the advantages of CS is that to reconstruct the signal of an actuator only one output of CS corresponding to that actuator is needed. In other words, the influence matrix that maps DM signals to CS outputs is supposed to be diagonal, and actuators are completely decoupled. If this is indeed the case, no matrix inversion and matrix-vector multiplication is needed for reconstruction, and the problem that required N^2 operations, where N is order of the DM, now requires only N operations.

To test this hypothesis, the mirror-sensor influence matrix is first calculated in simulation environment, and then measured in experimental setup. Recall the relation between actuator inputs $\mathbf{u}$ and CS output signals $\mathbf{c}$:

$$\mathbf{c} = R\mathbf{u},$$

where R is the influence matrix of the mirror-sensor pair. By direct analogy with previously explained SH influence matrix, the i^{th} column r_i of the matrix R is simply the output vector of CS when only i^{th} actuator is active and set to $+1$. This is precisely how influence matrix is simulated and measured. Each actuator of the DM is set to $+1$ one at a time, and output of CS is recorded and written as corresponding column of the influence matrix. The result of simulation is represented in Figure 3-10.

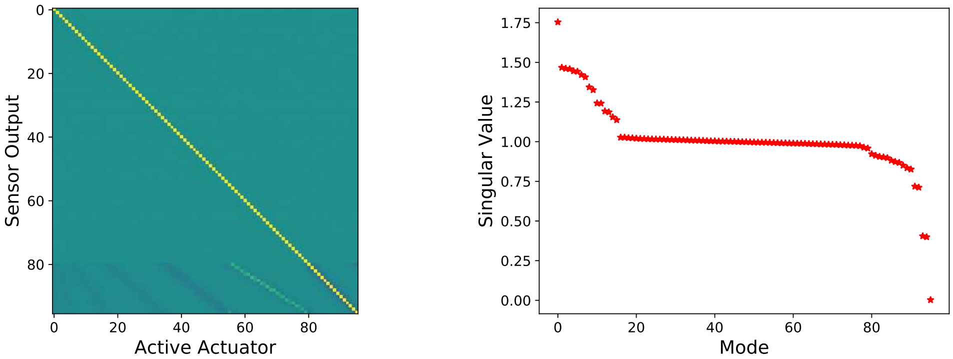

Figure 3-10: (left) Influence matrix of the curvature sensor paired to the membrane mirror, simulation. **(right)** Singular values of modes of the curvature sensor

Figure 3-10 (left) represents the simulated influence matrix, and (right) is the plot of its singular values. Here the resulting influence matrix is the average of matrices obtained in 200 simulations. This is needed in order to distinguish off-diagonal noise terms from true cross-talk. As it can be observed, the influence matrix has expected structure with dominant diagonal values. This means that each actuator produces intensity difference locally over its area, as expected from the theory. However, the boundary actuators suffer from cross-talk and cause smallest singular values to appear. The influence matrix becomes almost identity when all the boundary terms are removed. This can be seen from the matrix structure and its singular values, represented in Figure 3-11.

The cross-talk is even more pronounced in the influence matrix obtained from the experimental setup (Figure 3-12). Therefore using intensity information only to reconstruct signals on boundary actuators may lead to instabilities.

This result suggests that it is possible to use intensity-only reconstruction for the actuators not located on the boundary of aperture. Correction with boundary actuators is a more challenging problem and may require some modifications made to the sensor in Section 3-7, but first the method must be tested in closed loop on aberration generated from random actuator voltages as well as on an arbitrary aberration inserted into the system.

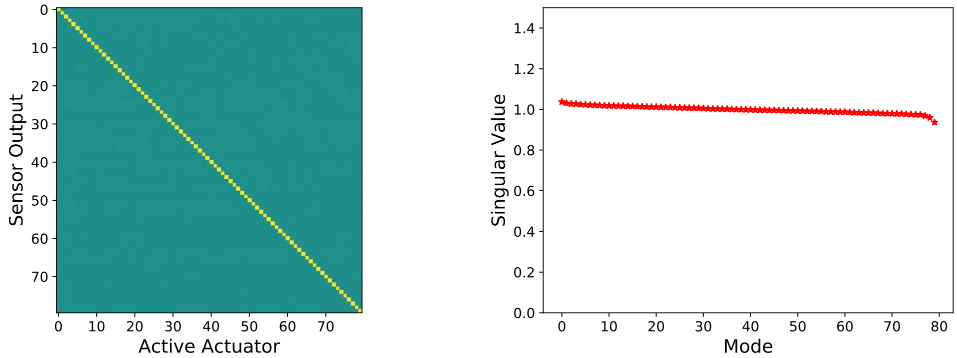

Figure 3-11: (left) Influence matrix of the curvature sensor paired to the membrane mirror obtained in simulation excluding terms corresponding to the boundary actuators. **(right)** Singular values of modes of the curvature sensor

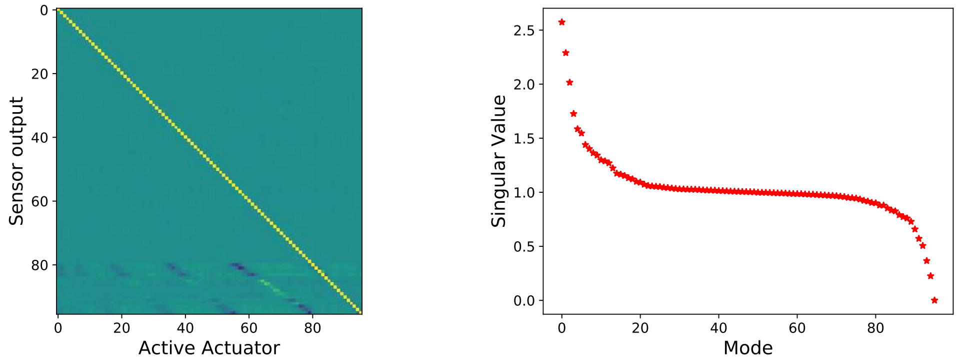

Figure 3-12: (left) Influence matrix of the curvature sensor paired to the membrane mirror, experiment. **(right)** Singular values of modes of the curvature sensor

3-6 Wavefront correction using only intensity information

In theory, a Curvature Sensor produces enough data to correct wavefront. Boundary actuators however introduce a significant amount of cross-talk into the system, and may lead to instabilities in reconstruction of actuator input signals. The goal of this section is to examine the significance of this effect and its influence on correction quality. The tests are performed in both simulation and experimental setup, with all configurations remaining unchanged.

First, the method is tested in simulation on an aberration defined as a linear combination of the mirror influence functions. For this the actuator inputs $\mathbf{u}$ are set to random values, such that $u_i \in [-1, 1]$. This static aberration is corrected in closed loop with feedback coefficient $k_{fb} = 0.3$ for 30 iterations. The simulation is repeated for 50 trials. The result is represented in Figure 3-13.

The mean value and the variance of $\|\mathbf{u}\|_2$, taken over the 50 random voltage sets (y-axis), is plotted against closed loop iteration number (x-axis). It can be observed that in simulation it is possible to correct mirror-generated static aberration, and boundary actuators do not

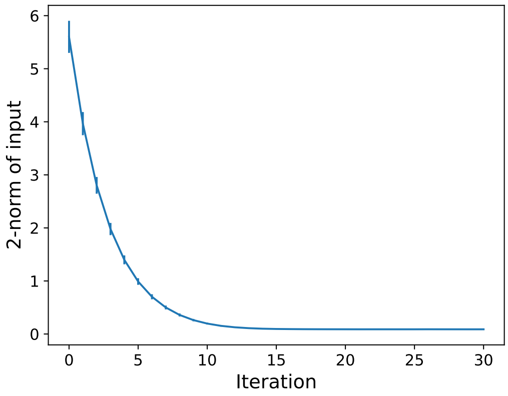

Figure 3-13: Correction of static aberration generated by setting mirror actuators to random voltages, simulation. The x-axis represents iteration number, the y-axis represents 2-norm of the actuators voltage.

produce any difficulties. In general, good performance in simulation environment does not guarantee convergence in real setup, and therefore the same tests must be repeated in experiment. The result is represented in Figure 3-14.

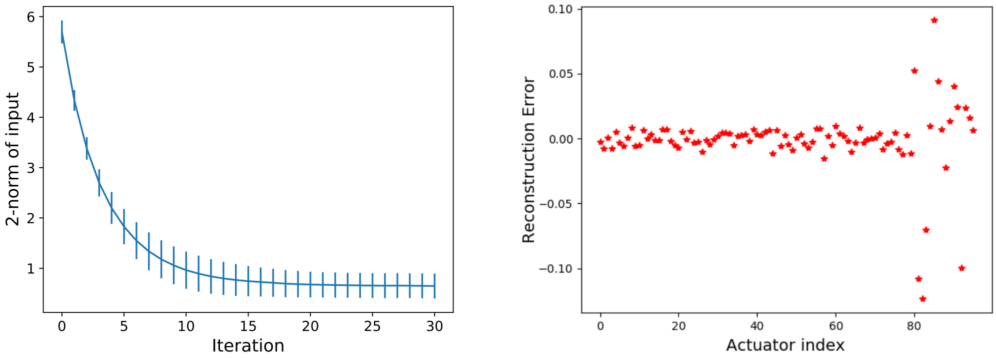

Figure 3-14: (left) Mean and variance of 2-norm of actuator inputs plotted against iteration number, simulation. **(right)** Typical actuator signal at the last step of correction, experiment

Figure 3-14 (left) represents mean and variance of $\|\mathbf{u}\|_2$ for the 50 trials. Figure 3-14 represents typical $\mathbf{u}$ at the last step of correction. In Figure 3-15 the image obtained with CS is shown before (left) and after (right) correction. As it can be observed, the image is highly non-uniform before the correction with intensity modulations having actuator shapes. From Figure 3-14 it can be observed that the method works in experimental environment, but the performance of correction is reduced for the boundary actuators, as expected. The reason is the cross-talk in this region and diffraction on the aperture boundary. Performance decrease is within the expected limit, and therefore the method can be tested in correcting arbitrary wavefront aberration in experimental setup. To do this, a transparent disk with hairspray layer of varying thickness is placed in the beam path. The correction is performed using all mirror actuators. In attempt to remove the issues associated with boundary actuators,

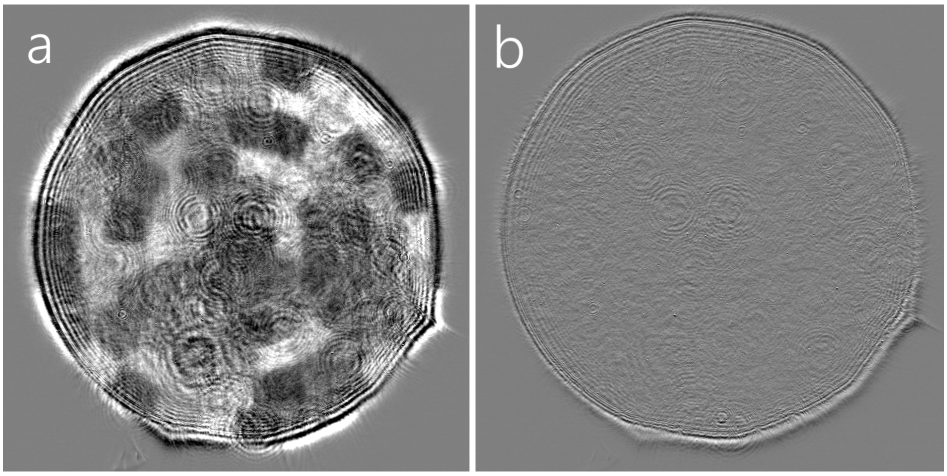

Figure 3-15: Experiment with correction of random voltages on the mirror actuators: **a** Initial intensity distribution has clear non-uniformities, **b** Final intensity distribution is almost flat, corresponding to wavefront with zero curvature.

another experiment is performed where the aberration is corrected using 80 actuators inside the footprint away from the boundary. For comparison the aberration is corrected using SH sensor. In all cases, SH Wavefront Sensor (WFS) is used to measure the residual aberration. The result of this experiment is represented in Figure 3-16.

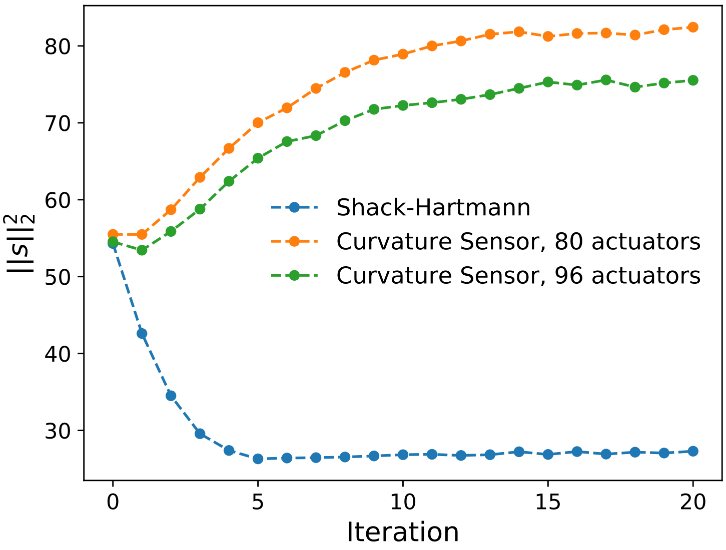

Figure 3-16: Correction of general aberration introduced into the system. The experiment is performed 3 times: CS using 80 actuators, CS using 96 actuators, and using SH sensor.

The x-axis represents the iteration number and the y-axis represents $\|\mathbf{s}\|_2^2$, where $\mathbf{s}$ is vector of centroid displacements measured by SH. In this experiment lens L4 has focal length $f = 70\,\mathrm{mm}$. In Figure 3-16 divergent behavior is observed for CS correction, both in 96 and 80 actuator setting. The reason is high sensitivity of the intensity-based correction to experimental setup imperfections. Therefore the method requires modifications to improve robustness, and these are introduced in the nest section.

3-7 Combined curvature and gradient correction

Setting correct boundary conditions on the mirror purely from intensity measurement is experimentally challenging problem. An alternative is to complement the curvature measurements with gradient measurements performed by a Shack-Hartmann sensor. In the proposed method the control zones are split between curvature and Shack-Hartmann sensor as it is schematically represented in Figure 3-17.

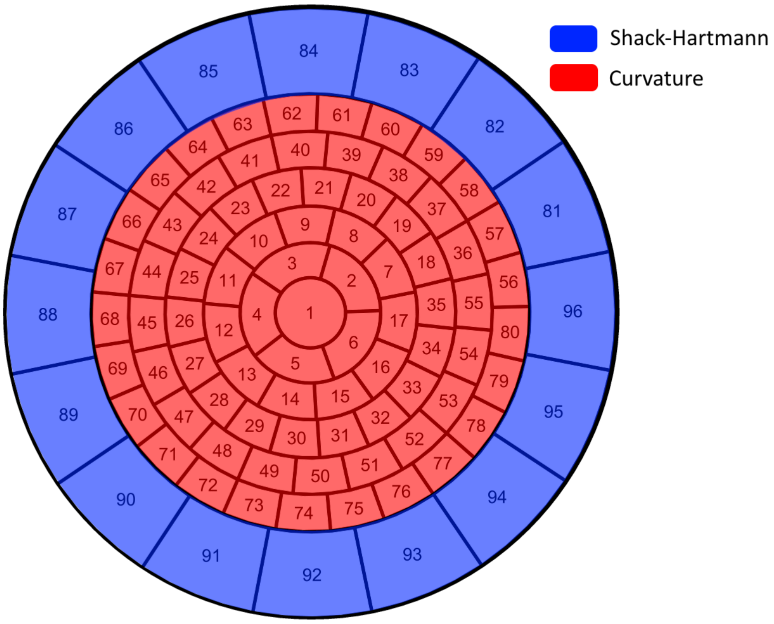

Figure 3-17: Division of correction zones. Central actuators (red) are controlled by the curvature sensor, boundary actuators (blue) are controlled by the Shack-Hartmann sensor.

The n_c actuators inside the beam footprint are controlled by the curvature sensor as described before. These actuators are further referred to as central. The n_b actuators on the boundary are controlled separately by the Shack-Hartmann sensor using only annulus of n_{ml} centroids located at the boundary (see Figure 3-18). These actuators are further called boundary actuators.

Let $\mathbf{c}$ be the vector of curvature measurements inside the beam footprint, satisfying

$$\mathbf{c} = R\mathbf{u_1},$$

where $R \in \mathbb{R}^{n_c \times n_c}$ is the curvature sensor influence matrix for the central actuators, and $\mathbf{u_1} \in \mathbb{R}^{n_c \times 1}$ is vector of inputs to the actuators in the controlled region. As it was shown before, R has dominant diagonal terms. Since here only central actuators are controlled by the curvature sensor, R does not contain the cross-talk terms, and the assumption $R = I$ can

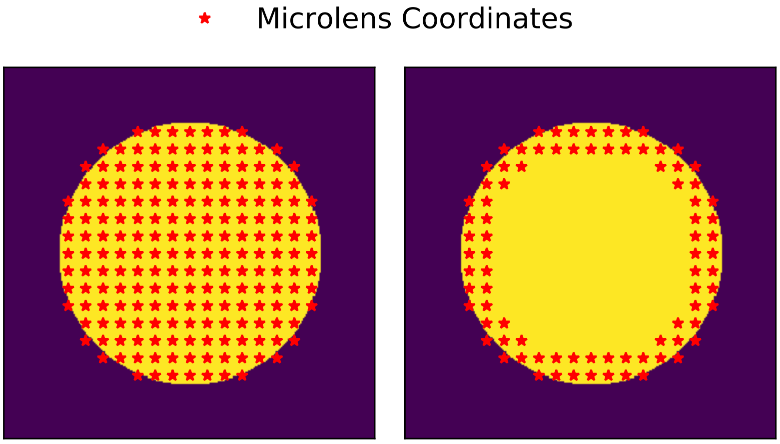

Figure 3-18: Example of positions of microlenses in the annular region near the boundary, used to control the boundary actuators.

be made, where $I \in \mathbb{R}^{n_c \times n_c}$ is the identity matrix. Let $\mathbf{s}$ be the slope measurements at the edge of the aperture, then $\mathbf{s}$ satisfies

$$\mathbf{s} = \begin{bmatrix} X & H \end{bmatrix} \begin{bmatrix} \mathbf{u_1} \\ \mathbf{u_2} \end{bmatrix},$$

where $H \in \mathbb{R}^{n_{ml} \times n_b}$ is the SH influence matrix mapping the voltages on boundary actuators to movements of boundary centroids, $X \in \mathbb{R}^{n_{ml} \times n_c}$ is the SH influence matrix mapping voltages on central actuators to movements of the boundary centroids, and $\mathbf{u}_2 \in \mathbb{R}^{n_b \times 1}$ is the vector of inputs to the boundary actuators. In order to combine readings of the two sensors, the individual influence matrices are normalized by the largest singular value to satisfy

$$\frac{\mathbf{c}}{\sigma_r} = \frac{1}{\sigma_r} R\mathbf{u_1}, \tag{3-7}$$

$$\frac{\mathbf{s}}{\sigma_s} = \frac{1}{\sigma_s} \begin{bmatrix} X & H \end{bmatrix} \begin{bmatrix} \mathbf{u_1} \\ \mathbf{u_2} \end{bmatrix}, \tag{3-8}$$

where σ_r is the largest singular value of matrix R and σ_s is the largest singular value of matrix $[X \quad H]$. When further referring to $\mathbf{c}$, $\mathbf{s}$ and the corresponding matrices, their normalized versions are meant. Normalized measurements from the two sensors are combined into a single vector, satisfying:

$$\begin{bmatrix} \mathbf{c} \\ \mathbf{s} \end{bmatrix} = \underbrace{\begin{bmatrix} I & 0 \\ X & H \end{bmatrix}}_{B} \begin{bmatrix} \mathbf{u_1} \\ \mathbf{u_2} \end{bmatrix}, \tag{3-9}$$

and used for control. In general, matrix $X \neq 0$ since central actuators also produce centroid movements. For now the assumption $X = 0$ is made, which is realistic for high order deformable mirrors with localized actuator influence functions, and the control between the two zones is therefore split, as it is seen from Equation (3-10).

$$\begin{bmatrix}\mathbf{c}\\ \mathbf{s}\end{bmatrix} = \underbrace{\begin{bmatrix}I & 0\\ 0 & H\end{bmatrix}}_{A}\begin{bmatrix}\mathbf{u_1}\\ \mathbf{u_2}\end{bmatrix}. \tag{3-10}$$

The implications of this assumption are analyzed later in more details. From the experiment it was observed that including $X \neq 0$ into matrix A produces only marginal improvement. Assumptions $R = I$ is justified by the fact that this substitution leaves singular values of the resulting influence matrix almost unchanged, as observed in Figure 3-19.

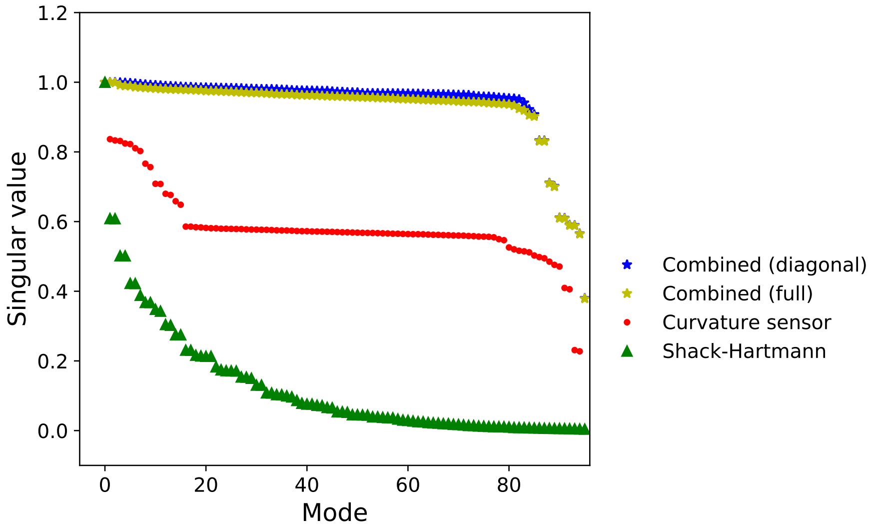

Figure 3-19: Normalized singular values of combined influence matrix plotted against singular values of Curvature Sensor and Shack-Hartmann sensor influence matrices.

Here, Combined means combined curvature-gradient WFS, full is matrix A with CS influence matrix R containing off-diagonal terms, and diagonal is A after substitution $R = I$ is made. In Figure 3-19 it can also be observed that the singular values of matrix A fall off significantly slower than for other methods. This means improved matrix condition number, and better stability and robustness upon inversion with respect to the original CS. The input signals are calculated as

$$\mathbf{u} = A^{\dagger}\begin{bmatrix}\mathbf{c}\\ \mathbf{s}\end{bmatrix},$$

where $\cdot^{\dagger}$ denotes pseudo-inverse. The combined matrix is inverted using SVD decomposition with singular values $\sigma < k_{\sigma}\sigma_0$ dropped. The inverse of the influence matrix is represented in

Figure 3-20.

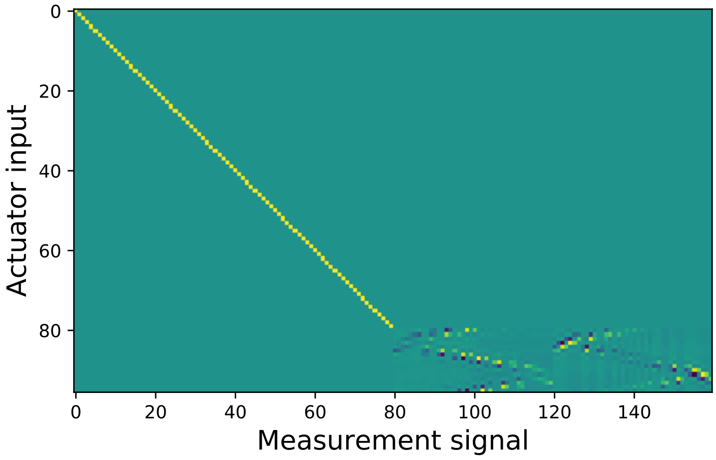

Figure 3-20: Inverse influence matrix of combined sensor obtained in simulation - the dominant diagonal structure for the central actuators suggests that only one curvature signal c_i can be used to calculate the correction voltage u_i.

The resulting inverted influence matrix $A^\dagger$ exhibits the expected structure. Inner actuators are controlled by CS only and each requires only one corresponding measurement, while 16 actuators at the boundary are controlled by the SH sensor. Therefore, a combined curvature and gradient sensing method preserves the diagonal influence matrix structure for inner actuators, and is expected to be more robust and perform better in reconstructing signals for boundary actuators, as the singular values of the influence matrix suggest.

3-7-1 Correction with boundary centroids

The proposed method is evaluated in simulations and experimental setup. First, it is necessary to determine the optimal lower bound for singular value. For this, the following simulation is performed. Actuators are set to random initial voltages, and the values are calculated iteratively. This procedure is repeated for 100 times. The optimal singular value lower bound k_σ is the one that minimizes error in reconstructed voltages. The mean and variance of reconstruction error for $k_\sigma = 0.4$ (1 mode dropped) and $k_\sigma = 0.6$ (4 modes dropped) is represented in Figure 3-21.

It is observed that dropping more than 1 mode increases the reconstruction error for the boundary actuators. Thus the optimal performance is achieved when 1 mode with smallest singular value is dropped, which sets $k_\sigma = 0.4$.

In order to investigate the performance of the proposed method and compare it with pure CS-based AO and SH-based AO, the following simulation is performed. An aberration rep-

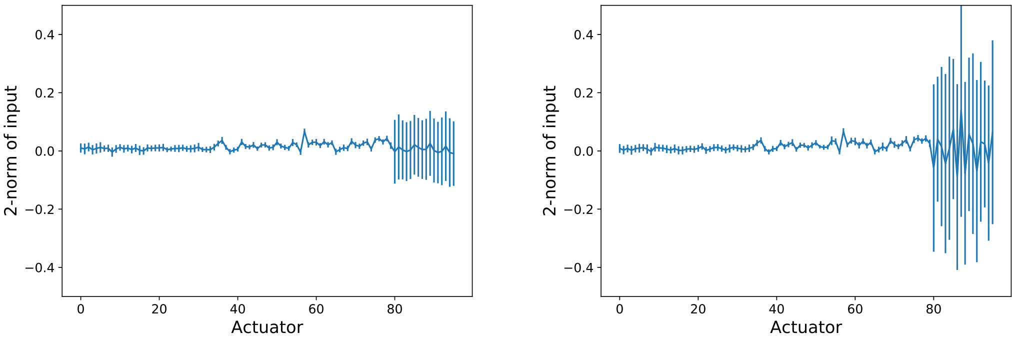

Figure 3-21: Mean and variance of correction error for each actuator for 100 random voltage sets, **(left)** $k_\sigma = 0.4$, **(right)** $k_\sigma = 0.6$

resenting atmospheric turbulence phase screen is generated using Zernike polynomials up to radial order degree $n = 10$, with tip, tilt and piston terms removed. The aberration is corrected in 30 steps with feedback coefficient $k_{fb} = 0.5$ using the compared methods. The RMS value of residual phase in radians is recorded as a function of iteration number, and then steady state average value is calculated for the last 20 correction steps. The simulation is repeated for 100 random turbulence phase screens, and the result is represented in Figure 3-22.

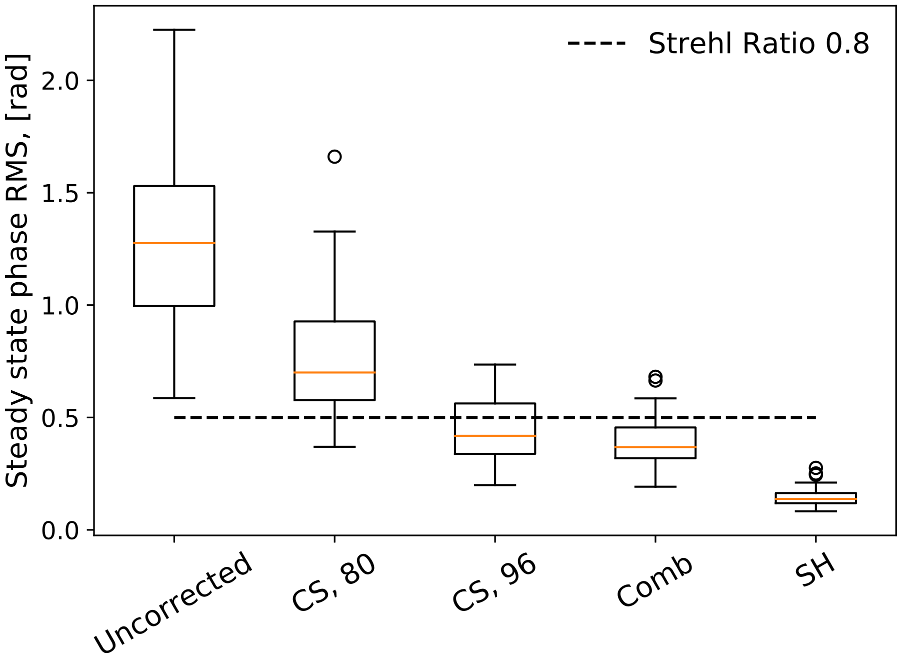

Figure 3-22: Simulation results of correcting 100 random turbulence realizations with different methods.

Here, CS, 80 and CS, 96 are corrections with intensity-based Curvature Sensor using 80 and 96 actuators, respectively, Comb is proposed combined curvature and gradient-based method and SH is correction with Shack-Hartmann sensor only. It can be observed that correction with CS converges in simulation, unlike in experimental environment, but this is of little practical significance since the method was observed to be divergent in experiment before. The proposed method improves correction compared to the intensity-based CS, and is more stable in experimental setting, as it is shown later. The performance is comparable with SH sensor, but the influence matrix and its inverse are diagonal for the inner actuators. Therefore, the advantage of this method is easy applicability to high-order DM, where the amount of inner actuators N_i is much larger than boundary actuators N_b. In order to calculate inputs $\mathbf{u} \in \mathbb{R}^{(N_i+N_b)\times 1}$ using SH sensor with $n_{ml} = (N_i + N_b)$ microlenses, the number of required operations is $N_{op,sh} \propto (N_i + N_b)^2$. For CS the diagonal structure of inverse influence matrix reduces the amount of operations to $N_{op,cs} \propto N_i + N_b^2$. In the limiting case of high order DM with $N_i \gg N_b$ $N_{op,sh} \propto N_i^2$, whereas $N_{op,cs} \propto N_i$. Therefore the method increases speed of computational stage of correction significantly for high order deformable mirrors.

The method is tested in the experimental setup on set of random aberrations. The aberrations are corrected using CS with 96 and 80 actuators, proposed combined curvature and gradient sensor and SH WFS for reference, with feedback coefficient $k_{fb} = 0.5$. The variance of measured centroid displacements is recorded at every correction step, and plotted against iteration number. A representative example of correction is in Figure 3-23.

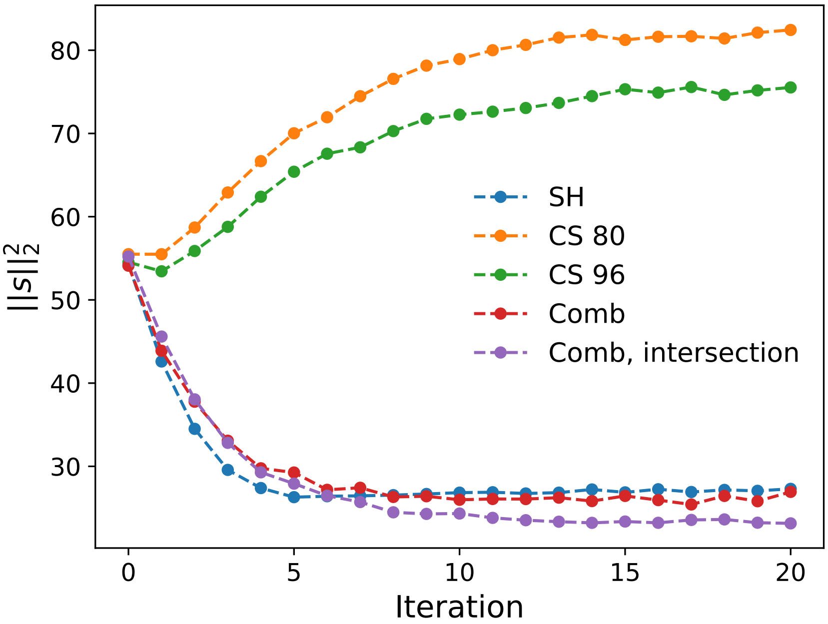

Figure 3-23: A representative experimental result of random aberration correction. Here, (CS, 80) is curvature sensor using only 80 central actuators, (CS, 96) is curvature sensor using all mirror actuators, (SH) is Shack-Hartmann sensor, (Comb) is the combined curvature and gradient sensor, controlling inner actuators and boundary actuators separately, and (Comb, intersection) is the combined curvature and gradient sensor, where influence matrix includes centroid displacements for actuators 55-80.

The correction was performed with several methods for comparison. Here, CS, 96 is compensation using curvature sensor and all mirror actuators, CS, 80 is curvature sensor and 80 central actuators, SH) is Shack-Hartmann sensor, Comb is combined curvature and gradient sensor (proposed method), and (Comb, intersection) is proposed method with centroid displacements for actuators 55-80 included into influence matrix, which is one more ring of actuators before the boundary. It can be observed that controlling additional ring of actuators with Shack-Hartmann sensor improves the correction only slightly.

Therefore, the proposed combined curvature and gradient method shows convergence in experimental setup, unlike pure CS. The performance of correction is comparable to the one achieved with SH, and the computational costs are greatly reduced. Increasing the DM order will increase necessary SH microlenses density and computational costs such that at some point SH will become impractical to use. Proposed method does not suffer from this complication, since wavefront sampling is effectively performed by each individual pixel, and actuator response is decoupled.

3-7-2 Effect of image resolution on performance

The experimental setup used in this thesis is such that every mirror actuator is imaged by a large amount of camera pixels. In high order deformable mirrors where the presented method yields best speed improvement, this may not be the case. In order to see how the number of pixels per actuator influences the correction, the following experiment is conducted. Mirror voltages are set to initial random values, which are corrected in closed loop with $k_{fb} = 0.5$, using full CS influence matrix containing off-diagonal terms, and using sparse matrix containing diagonal terms only. The intensity distribution used to calculate curvature signals to close the loop is downsampled by 2^m, where $m \in \mathbb{Z}, 0 \leq m \leq 5$. The variance of the measured centroid displacements in pixels is calculated and plotted against iteration number (Figure 3-24, upper figures). Mean and standard deviation of the centroid displacement variance in steady state is represented in Figure 3-24, bottom figure.

The following observations are made from this experiment. First, decreasing the number of pixels of CS per mirror actuator does not reduce the correction performance. Areas as small as 4×4 pixels can be used to calculate required control signal, which confirms the applicability of proposed method to high-order DM. Second, the quality of closed loop correction using full CS influence matrix and using only its diagonal terms is the same within experimental uncertainty. This observation confirms theoretical considerations and simulation results.

3-7-3 Analysis of cross-talk influence of the sensor performance

During the experiments on sensor performance, the effect of central actuators on boundary centroids was assumed to be zero. While it is possible to minimize it, for instance by operating high order DM with the localized first derivatives of the actuator influence functions or selecting centroids on the boundary sufficiently far from central actuators, in general the cross-talk term in the combined influence matrix is nonzero. In this section the effect of the assumed approximation is analyzed in more details.

Recall the matrix equation for the combined sensor Equation (3-9):

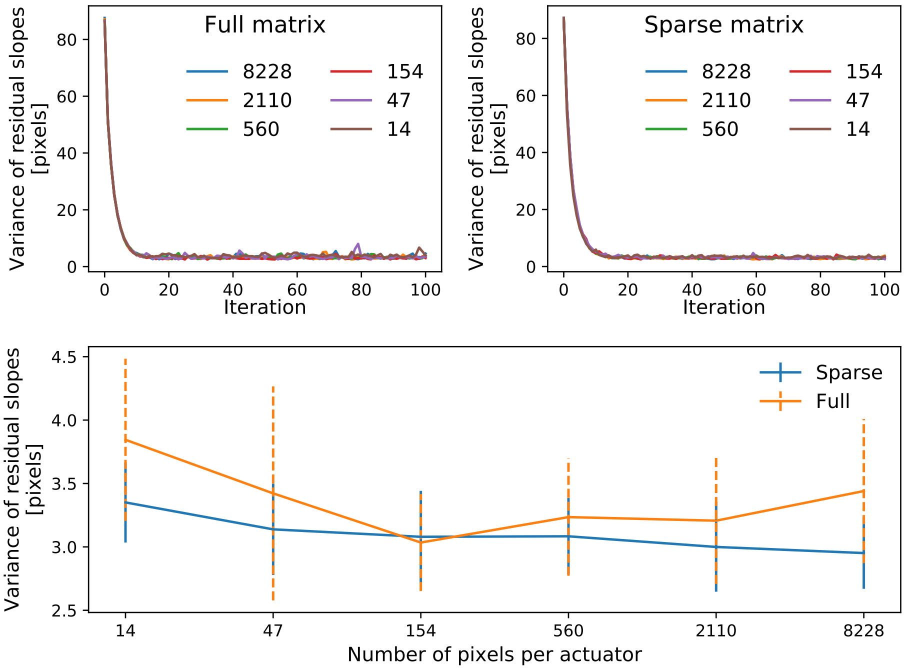

Figure 3-24: Results of random voltage correction in closed loop depending on the amount of pixels per actuator.

$$\begin{bmatrix} \mathbf{c} \\ \mathbf{s} \end{bmatrix} = \begin{bmatrix} I & 0 \\ X & H \end{bmatrix} \begin{bmatrix} \mathbf{u_1} \\ \mathbf{u_2} \end{bmatrix}, \tag{3-11}$$

where $R = I$ is the normalized curvature sensor influence matrix for the central actuators, assumed to be identity, H is normalized SH influence matrix for boundary actuators, and X is the coupling term representing effect of central actuators on the boundary centroids.

Because of the structure of the combined influence matrix B it is easy to diagonalize it:

$$\underbrace{\begin{bmatrix} I & 0 \\ -X & I \end{bmatrix}}_{T} \underbrace{\begin{bmatrix} I & 0 \\ X & H \end{bmatrix}}_{B} = \underbrace{\begin{bmatrix} I & 0 \\ 0 & H \end{bmatrix}}_{D}. \tag{3-12}$$

Therefore, a linear combination of combined sensor output essentially diagonalizes the resulting influence matrix:

$$B\mathbf{u} = \mathbf{b}, \tag{3-13}$$

$$TB\mathbf{u} = T\mathbf{b}, \tag{3-14}$$

$$D\mathbf{u} = \mathbf{b}', \tag{3-15}$$

$$\hat{\mathbf{u}} = D^{\dagger}\mathbf{b}', \tag{3-16}$$

and pseudo-inverse of matrix D is

$$D^{\dagger} = \begin{bmatrix} I & 0 \\ 0 & H^{\dagger}. \end{bmatrix} \tag{3-17}$$

Working with the linear transformation of measurements increases the number of operation slightly, adding additional $\approx N$ operations, where N is the number of sensor measurements and is assumed to be order of actuator number. It still remains interesting to observe how X affects correction performance and for this the following simulation is performed. Aberration correction for different number of actuators included in the intersection term X is simulated for 30 iterations and is repeated for 100 different phase screens. For this, a certain number of leftmost columns of matrix X are set to 0, meaning that a definite number of inner actuator rings are assumed to have no effect on centroid movements. The wavefront phase RMS value in steady state is recorded for every screen and every number of actuators in the coupling term X. The result is represented in Figure 3-25.

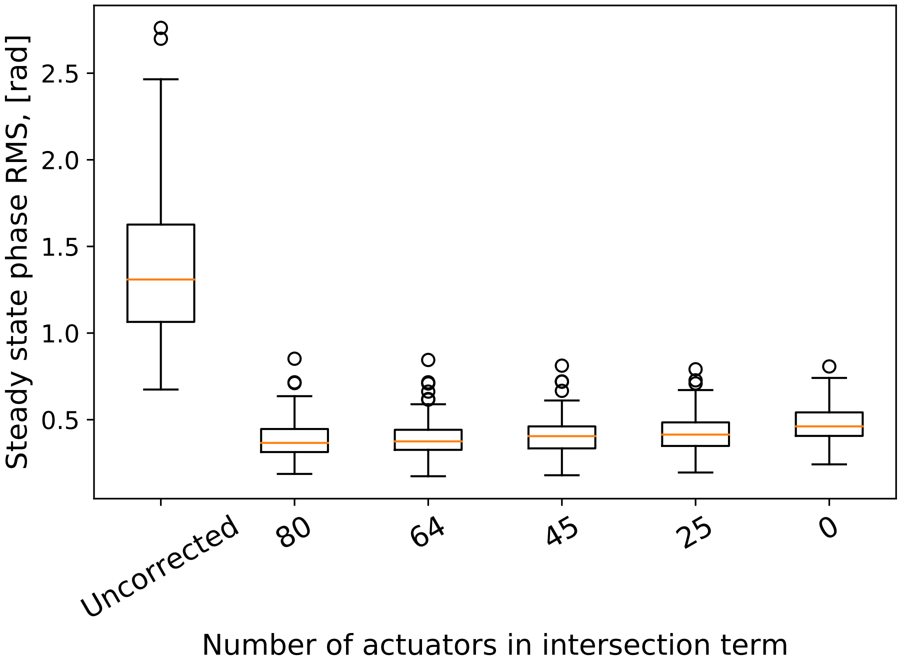

Figure 3-25: Results of simulation of atmospheric turbulence correction with different amount of actuators included in the coupling term X.

Here the x-axis is labeled according to number of actuators included in the coupling term X. It can be observed that using complete influence matrix B improves correction only negligibly. Mean residual aberration RMS in case of full coupling term is 28.5 % of the initial value, and 34.5 % in case of completely decoupled control, which means 6 % improvement. Therefore, it is possible to either diagonalize the influence matrix at the cost of computational speed, or to sacrifice a certain amount of correction quality and simply neglect the terms that couple inner actuator rings to boundary SH centroids.

3-8 Application of correction with Curvature Sensor to the high-order KiloDM

The final experiment to be performed is wavefront correction with Curvature Sensor paired with high order DM. As mentioned in Section [**?**], the method yields largest benefit on this type of device, eliminating the need of lengthy multiplications of full matrix by a vector. For this purpose experimental setup with CS and 952-actuators Boston Micromachines Kilo-DM [30] (Figure 3-26) is built.

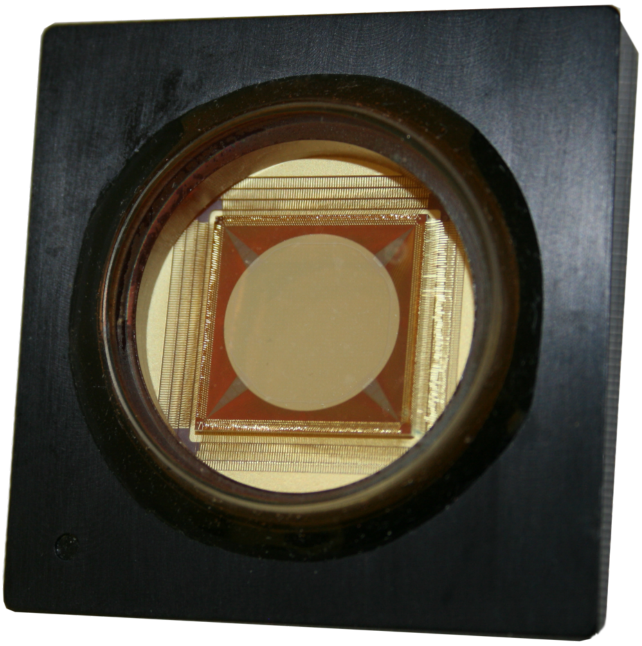

Figure 3-26: Boston Micromachines 952-atuators Kilo-DM.

The experimental setup is represented in Figure 3-27.

Here, (S) denotes light source, which is $\lambda = 472\,\mathrm{nm}$ LED coupled to $50\,\mu\mathrm{m}$ multimode fiber. Collimated beam hits transparent plate with aberration (AB), which is conjugated to the Deformable Mirror plane (DM) through the telescope composed of lenses L1 (100 mm focal) and L2 (100 mm focal). The mirror plane is conjugated to the Shack-Hartmann (SH) sensor through the telescope composed of lenses L3 (150 mm focal) and L5 (60 mm focal), and to the camera C1 through the telescope composed of lenses L3 and L4 (60 mm focal). Camera C1 captures uniform intensity distribution I_0. Camera C2 is located $z_0 = 3.6\,\mathrm{mm}$ further than camera C1 along the optical axis and captures the modulated intensity distribution I_{z_0}.

Initially each individual actuator displacement depends quadratically on applied voltage [30],

$$z = aV^2, \tag{3-18}$$

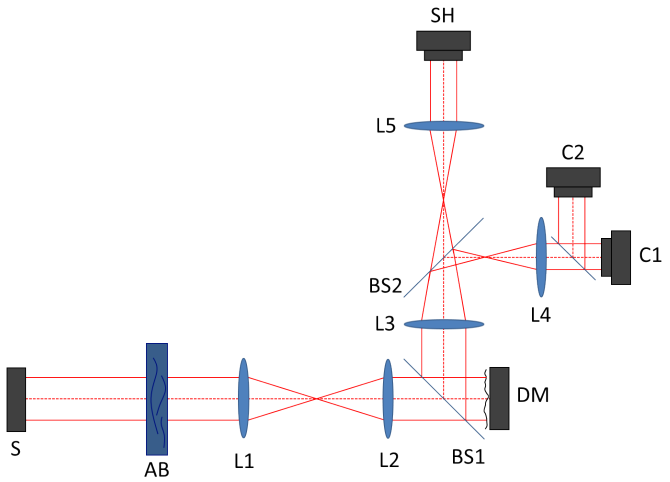

Figure 3-27: Experimental setup to evaluate performance of Curvature Sensor paired with high-order kilo-DM.

where V is applied voltage. To operate the mirror signal u which is linear with actuator displacements and varying between -1 and 1 must be calculated. Signal $u = 0$ corresponds to flat mirror voltage distribution, which is given by the manufacturer and is approximately equal to

$$V_{flat} = \frac{V_{max}}{\sqrt{2}} \tag{3-19}$$

for every actuator. Given the above listed properties of the linearized signal, it can be found as

$$u = 2\frac{V^2}{V_{max}^2} - 1, \tag{3-20}$$

and it is related linearly to the actuator displacement. In practice it is better not to use the full scale of allowed voltages and to limit $V \approx 0.7V_{max}$, mainly because actuator displacements do not follow Equation (3-18) near V_{max}. Figure 3-28 represents sample output image from the Curvature Sensor when with subtracted flat mirror intensity distribution. Individual actuators are easily observed.

Using the calibration procedure described in Section 3-1, the mirror influence matrix represented in Figure 3-29 is measured. The expected dominant diagonal structure can be observed. However in this case coupling between actuators is stronger than in case of membrane mirror with large actuators, because of the densely packed actuator geometry in this case. Inactive mirror actuators or regions with dust particles yield sensor output 1 for every active actuator and can be easily excluded from operation, although this is not necessary.

An important aspect of operating Kilo-DM with CS must be stressed. For the previously operated membrane mirror with fixed edges setting all actuators to the same voltage yields a

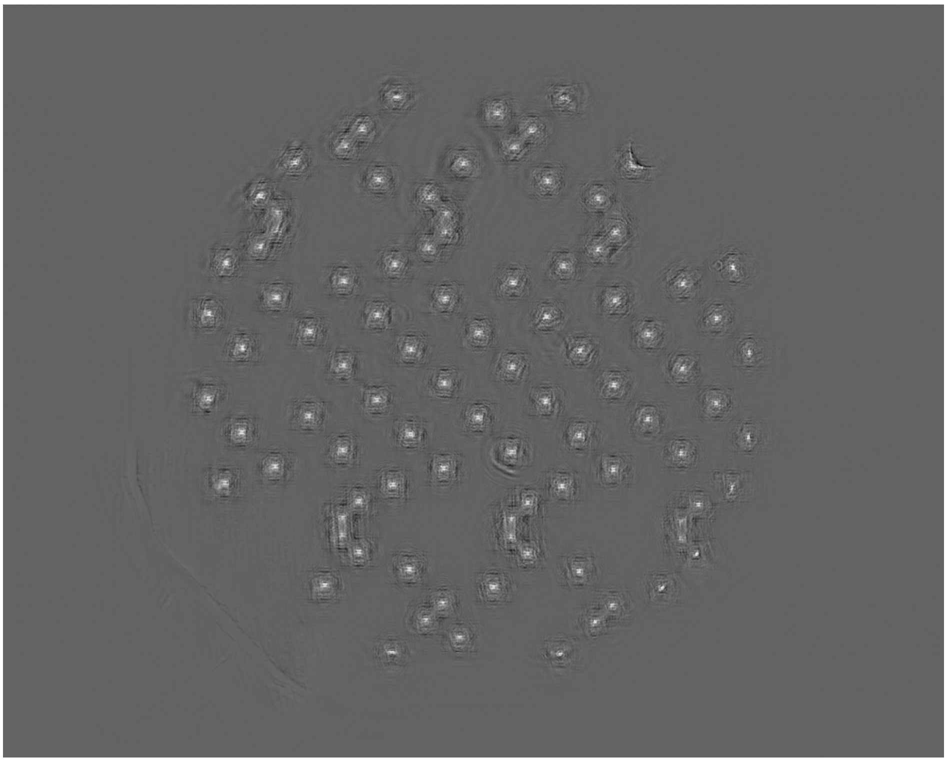

Figure 3-28: Example output image from the Curvature Sensor with subtracted image corresponding to flat mirror. Localized actuator response is easily observed.

defocus term, to which CS is sensitive. In the case of Kilo-DM setting actuators to the same voltage yields piston term in the largest part of the area. Neither SH, nor CS are sensitive to piston mode, and because of this the sensor output will be as if the mirror was at zero input level. Due to this the actuators may saturate quickly, and to prevent it the mean value of actuator voltages is subtracted at every correction iteration.

To evaluate performance of the CS with Kilo-DM the experimental setup represented in Figure 3-27 is used. A transparent disk with optical aberrations is inserted into the system. The aberrations are measured by SH sensor as centroid displacements vector $\mathbf{s}$. To evaluate correction quality, tip and tilt terms are removed from $\mathbf{s}$ by subtracting mean value of centroid displacements in each direction, and standard deviation σ_s is calculated. The feedback coefficient $k_{fb} = 0.5$ and the correction is performed for 30 iterations. The experiment is repeated for 10 different aberrations. Mean and standard deviation of σ_s is plotted against iteration number.

The x-axis in Figure 3-30 represents the iteration number of correction, the y-axis represents the standard deviation of SH output $\mathbf{s}$, σ_s, with tip and tilt terms removed. As it can be observed, CS is able to correct the aberrations in this case, as σ_s decreases over iterations, unlike in case of membrane mirror. A possible reason is much higher locality of influence functions of Kilo-DM actuators with only 15% interactuator coupling, which is worse for OKO membrane mirror. However, the problem of finding exact conditions when the method performs well is still to be solved, and presents an interesting research topic by itself.

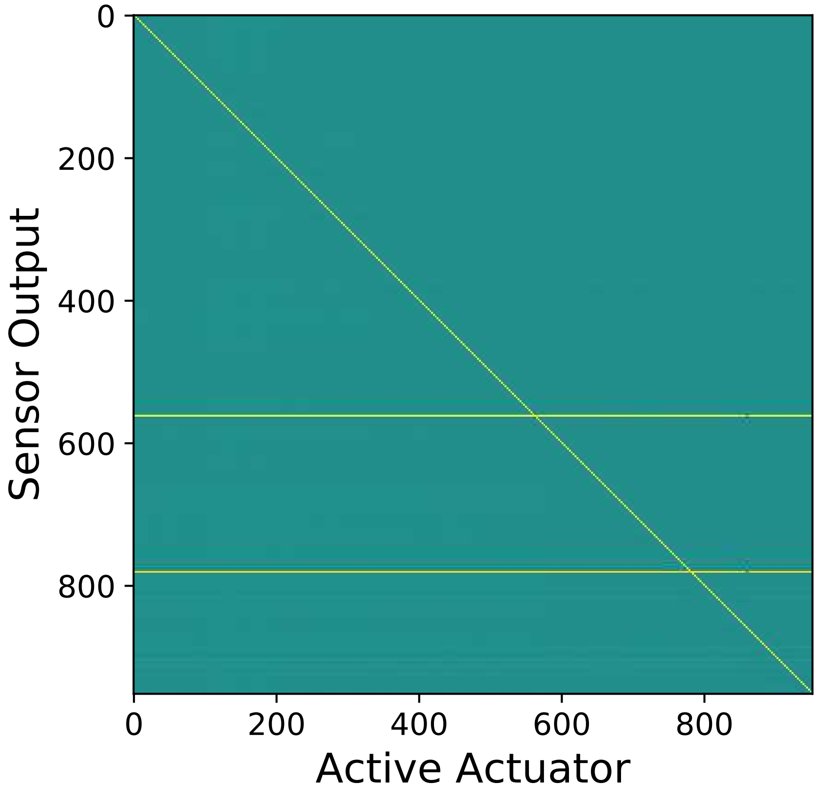

Figure 3-29: Measured KiloDM influence matrix. The expected dominant diagonal terms are observed. Broken actuators can be observed as well as the lines where sensor readings are 1 for every actuator.

From Figure 3-30 it can be observed that the variance of centroid displacements σ_s decreases, but does not approach zero with iterations. A possible reason is that this correction quality is limited by the mirror, and the rest of the modes cannot be corrected. Another possibility is that the correction quality is given by the fact that curvature sensor is less sensitive to low-order Zernike modes. As explained in Section Section 2-3-5, for a phase given by a single-frequency sinusoid with wave number k, Laplacian is proportional to $|k|^2$. Low order Zernike components contain mostly low spatial frequencies for which k is small, and therefore the sensor readings are dominated by high-order modes. The response of SH sensor is proportional to $|k|$ and detects lower order modes better than the CS. Curvature Sensor in the experiment was tuned by selecting the distance between the cameras z_0 to work in the linear region of the mirror actuators, which produce sharp and localized influence function containing high spatial frequencies. Therefore, the configuration was sensitive to high order aberration modes and much less sensitive to low-order modes which remained uncorrected, resulting in the relatively high residual phase variance.

Comparison with SH correction has not been made in this case, since the scope of this experiment is to show applicability of the method to high-order DM. In the used experimental setup each actuator had plenty of corresponding CS pixels. Therefore, it is possible to use it

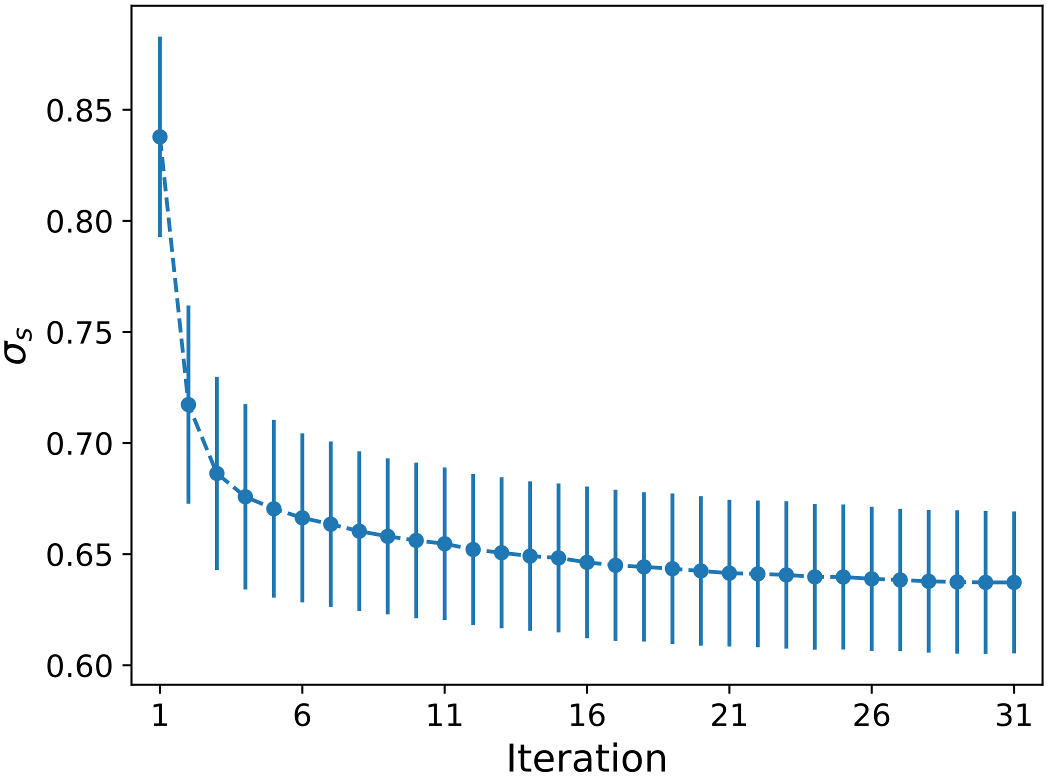

Figure 3-30: Results of aberration correction with Kilo-DM and Curvature Sensor. The x-axis represents number of correction step, the y-axis represents standard deviation of SH output with tip and tilt terms subtracted.

with even higher order DM. At some point the problem scale will become such that SH is unusable because necessary lenslet array is too dense to be produced. In this setting CS is still usable since camera pixels are mush smaller than any possible microlenses.

This section concludes using Curvature Sensor for AO correction. It was demonstrated to work with high-order 952-actuator DM. The expected properties are observed, namely diagonality of influence matrix, local actuator responses and fast correction. In the next section another application of CS is studied.

3-9 Wind velocity measurements

In astronomical observations the main source of time-varying aberrations is the atmospheric turbulence. Naturally occurring small variations in temperature cause small changes in wind velocity, which produce fluctuations of air density and hence of optical refractive index. It has been shown that the turbulence power is concentrated in a number of discrete layers at certain heights.

Many mathematical models of atmospheric turbulence use Taylor Frozen Flow Hypothesis (TFFH). It assumes the turbulence layers to have stationary frozen structure during the time it takes the layer to travel across telescope aperture. Therefore, statistical properties of atmospheric turbulence, such as Fried parameter r_0 are assumed to be slowly varying, but depending on the wind velocity in a given layer. In order to use optimal AO control it is necessary to estimate atmospheric properties and wind speed measurement is used for this purpose. Wind speed estimate is also used in predictive control techniques, which are used to compensate delay in the feedback loop.

A number of methods has been developed to measure wind speed in astronomy. Doppler LIDAR techniques are used during astronomical site testing. For real time measurements wind sensors based on covariance function of amplitude atmospheric scintillations were suggested, speckle correlation technique has been developed, and a method based on intensity fluctuations was suggested. An alternative is to use data from a wavefront sensor that already exists in AO loop. Roopashree et.al. [31] used correlation maps of phase reconstructed from Shack-Hartmann wavefront sensor measurements. This solution includes unnecessary step of explicit phase reconstruction from slope measurements. Li [32] reconstructed wind velocity from gradient of SH slope measurements and analyzed performance of the estimator. However, the method is limited to measurements of wind velocities $w \lessapprox 1.2\,\frac{\text{subaperture}}{\text{frame}}$ and atmospheric conditions $r_0 > 0.75, \text{subaperture}$. Schöck and Spillar [33] identified wind velocity using correlation maps obtained with SH WFS output data and evaluated the method on measurements obtained from both simulation and real data.

The above discussed curvature wavefront sensor is suitable for wind velocity measurements as well. A similar technique to [33] is used. Let $\phi(\mathbf{r}, t)$ be the turbulence-induced aberration across the telescope aperture, where $\mathbf{r}$ is coordinate inside the aperture, and t is time. The Frozen Flow hypothesis is mathematically stated as

$$\phi(\mathbf{r}, t) = \phi(\mathbf{r} + \mathbf{w}\tau, t + \tau). \tag{3-21}$$

Here, $\mathbf{w}$ denotes projection of the wind velocity onto the plane of telescope aperture, and τ is time delay. The same relation holds for wavefront sensor output, in this case Laplacian of the phase:

$$\nabla^2\phi(\mathbf{r}, t) = \nabla^2\phi(\mathbf{r} + \mathbf{w}\tau, t + \tau). \tag{3-22}$$

Wind velocity is estimated using the method of correlation maps. For an arbitrary discrete sampled function $f(x, y, t)$ define correlation

$$\begin{aligned} A(\Delta x, \Delta y, \tau) &= \frac{\int f(x, y, t) f(x + \Delta x, y + \Delta y, t + \tau) dx dy dt}{\sigma_1 \sigma_2 O(\Delta x, \Delta y)} && \text{(3-23)} \\ &= \frac{\sum_{x=0}^{N-1} \sum_{y=0}^{N-1} \sum_{t=0}^{t_{max}-1-\tau} f(x, y, t) f(x + \delta_x, y + \delta_y, t + \tau)}{\sigma_1 \sigma_2 O(\Delta x, \Delta y)}, && \text{(3-24)} \end{aligned}$$

where $f(x, y, t)$ is sampled on a grid $N \times N$ pixels for t_{max} temporal sampling points, σ_1 is the standard deviation of $f(x, y, t)$, σ_2 is the standard deviation of $f(x + \Delta x, y + \Delta y, t + \tau)$ and $O(\Delta x, \Delta y)$ is aperture overlap function, $O(\Delta x, \Delta y) = P(x, y) \star P(x, y)$, $P(x, y)$ is the pupil function. Now, let $f(x, y, t)$ be the curvature wavefront sensor output at time t, i.e. the normalized difference of intensity distributions in two camera planes with reference (flat) distribution subtracted. Assuming frozen flow hypothesis holds, the correlation function $A(\Delta x, \Delta t, \tau)$ has a sharp peak at $\Delta x = w_x \tau$, $\Delta y = w_y \tau$, where w_x, w_y denote projection of $\mathbf{w}$ onto x and y axis of the wavefront sensor respectively. By computing $A(\Delta x, \Delta y, \tau)$ for $\tau \in [1, \tau_{max}]$ and tracking the position of correlation peak, the wind velocity is estimated. The algorithm the reads as follows:

1. Before estimating wind velocities, the time average value of each pixel is subtracted from the sensor readings to account for diffraction at the boundaries.

2. Compute $A(\Delta x, \Delta y, \tau)$ for $\tau \in [1, \tau_{max}]$.

3. For each $A(\Delta x, \Delta y, \tau)$ estimate the position of correlation peak. In order to do so $A(\Delta x, \Delta y, \tau)$ is approximated with Gaussian function by means of nonlinear least squares fit from Python optimization toolbox:

$$A(\Delta x, \Delta y, \tau) \propto e^{-\frac{(x-\mu_x)^2}{2\sigma_x^2} - \frac{(y-\mu_y)^2}{2\sigma_y^2}}. \tag{3-25}$$

   Computed optimal values of μ_x and μ_y are then taken as the position of correlation peak. Given the physics of the problem it is known that correlation peak for $\tau = 0$ is expected to be at $(0, 0)$, so this information is added to the computed data.

4. Given the position of correlation peak for a range of τ, the problem reads

$$\underbrace{\begin{bmatrix} x_0 \\ x_1 \\ \vdots \\ x_n \end{bmatrix}}_{\mathbf{x}} = \underbrace{\begin{bmatrix} \tau_0 & 1 \\ \tau_1 & 1 \\ \vdots & \vdots \\ \tau_n & 1 \end{bmatrix}}_{F} \begin{bmatrix} w_x \\ c \end{bmatrix} + \epsilon, \tag{3-26}$$

   where ϵ is the vector of residuals. The problem is in typical least squares form and the solution is

$$\begin{bmatrix} w_x \\ c \end{bmatrix} = F^{\dagger}\mathbf{x}, \tag{3-27}$$

   where $F^{\dagger}$ denotes pseudoinverse. From the physics of the problem it is known that $c \approx 0$, since for $\tau = 0$ correlation peak is expected at $(0, 0)$ position, and w_x is estimated wind velocity in x-direction. The same procedure applies for y-direction.

The method is evaluated in simulation environment. Turbulence phase screen movement due to wind velocity under frozen flow assumption is simulated by taking phase screen in a moving subregion of a bigger screen. The large phase distribution is simulated using the method described in [34]. Phase $\phi(x,y,t)$ induced by the atmospheric turbulence across aperture is assumed to be normally distributed. The covariance function $\left\langle \phi\phi^T \right\rangle$ is given, according to von Karman theory, by

$$C_\phi(r) = \left(\frac{L_0}{r_0}\right)^{\frac{5}{3}} \frac{\eta}{2} \left(\frac{2\pi r}{L_0}\right)^{\frac{5}{6}} K_{5/6}\left(\frac{2\pi r}{L_0}\right), \tag{3-28}$$

where r_0 is Fried parameter, L_0 is turbulence outer scale, $\eta = \frac{2^{1/6}\Gamma(11/6)}{\pi^{8/3}} \frac{24}{5} \Gamma(6/5)^{5/6}$ is a constant, r is the distance between two points where covariance is evaluated, and $K_{5/6}$ is modified Bessel function of third type. The phase screen is then generated as

$$\phi(x,y) = \mathcal{F}^{-1}\left[\mathbf{e}\mathcal{F}\left[C_\phi(r)^{1/2}\right]\right], \tag{3-29}$$

where $\mathbf{e} \sim \mathcal{N}(0,1)$. The aperture diameter is assumed to be $d = 1\,\mathrm{m}$ sampled on a square grid with $N = 64$ pixels on each side. The camera pixels are assumed to be square with side $d_p = 5.6\,\mu\mathrm{m}$, hence the magnification of the system is $M = 0.0003584$. Outer scale $L_0 = 20\,\mathrm{m}$, Fried parameter is $r_0 = 20\,\mathrm{cm}$. For curvature sensor simulation the displacement between two measurement planes is $\Delta z = 1\,\mathrm{mm}$ and $I_0 = 100$, such that the intensity $I_{\Delta z}$ is modulated between 0 and 200. In general, Δz is proportional to r_0 to obtain maximal sensor output. The intensity images are simulated with additive white noise $n_g \sim \mathcal{N}(1,3)$ and Poisson noise with $\lambda = \frac{k_{shot}}{255} I(x,y)$, where $I(x,y)$ is the registered intensity and $k_{shot} = 3$. It was observed that estimation error in $\hat{w}_x$ is independent on w_y applied, so $w_y = 0$ during the simulations, and $w_x \in [1,8]\frac{\text{pixels}}{\text{frame}}$. Wind velocities were reconstructed from a time series of 48 frames. The simulation was repeated for 100 phase screens and the RMS estimation error is represented against applied velocity in Figure 3-31.

Under perfect frozen flow conditions, the curvature WFS is able to produce accurate estimates with estimation error below 1%. This compares to the result of [31] for single layer turbulence model, and avoids the unnecessary step of phase reconstruction from the WFS measurements. Highest wind speed that is possible to estimate with curvature WFS is limited by the pixel number:

$$v_{max} = \frac{N - b}{2}, \tag{3-30}$$

where N is wavefront sensor dimension in pixels, and b is the boundary set in order to limit the region in which correlation is computed.

For perfect frozen flow turbulence the estimation accuracy does not depend on white noise covariance when enough measurements are made and correlation peaks occur at overlap values

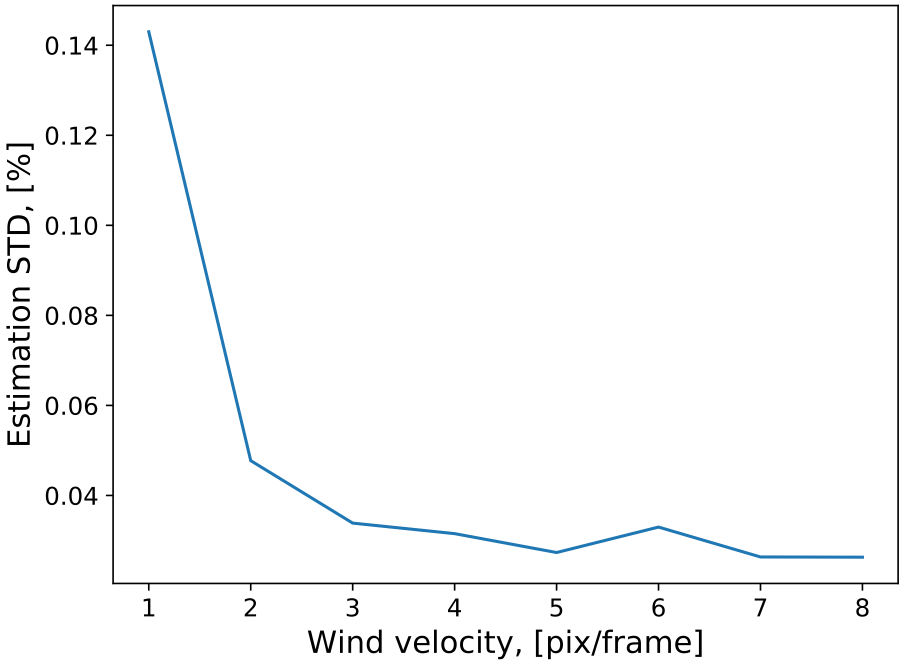

Figure 3-31: Wind velocity estimation error in [%] plotted against real wind velocity.

$\Delta x \ll N$, where N is sensor dimension in pixels. This means that there is a reasonably large number of pixels in the intersection region of two functions for which correlation is computed. Let the curvature sensor output be $\mathbf{c}(x, y)$, and additive white noise be $\mathbf{w}(x, y) \sim \mathcal{N}(0, \sigma^2)$. At two time instances, $t = t_0$ and $t = t_0 + \tau$, the sensor measurements are

$$\mathbf{c}_m(x, y, t_0) = \mathbf{c}(x, y, t_0) + \mathbf{w}_1, \tag{3-31}$$

$$\mathbf{c}_m(x, y, t_0 + \tau) = \mathbf{c}(x, y, t_0 + \tau) + \mathbf{w}_2, \tag{3-32}$$

where $\mathbf{c}(x, y, t)$ is the noiseless curvature signal. Under frozen flow assumption,

$$\mathbf{c}(x, y, t + \tau) = \mathbf{c}(x - \Delta x, y - \Delta y, t), \tag{3-33}$$

$$\mathbf{c}(x + \Delta x, y + \Delta y, t + \tau) = \mathbf{c}(x, y, t), \tag{3-34}$$

where $\Delta x = w_x\tau$, $\Delta y = w_y\tau$, and (w_x, w_y) is the projection of wind velocity vector onto the x and y-axis of the wavefront sensor. Combining these two equations results in

$$\mathbf{c}_m(x, y, t_0) = \mathbf{c}(x, y, t_0) + \mathbf{w}_1, \tag{3-35}$$

$$\mathbf{c}_m(x + w_x\tau, y + w_y\tau, t_0 + \tau) = \mathbf{c}(x, y, t_0) + \mathbf{w}_2. \tag{3-36}$$

Therefore,

$$\left\langle \mathbf{c}_m(x+\Delta x, y+\Delta y, t_0+\tau)^T \mathbf{c}_m(x,y,t_0) \right\rangle = \begin{cases} \left\langle \mathbf{c}^T\mathbf{c} \right\rangle + \sigma^2, & \Delta x = w_x\tau,\ \Delta y = w_y\tau, \\ \left\langle \mathbf{c}(x+\Delta x, y+\Delta y, t_0)\mathbf{c}(x,y,t_0) \right\rangle, & \text{otherwise,} \end{cases} \tag{3-37}$$

and a sharp peak is expected for $\Delta x = w_x\tau$, $\Delta y = w_y\tau$. Noise covariance σ only increases height of the peak and therefore does not affect estimation accuracy. For a real measurement however there is a finite non-zero probability P_w of having a peak in correlation function at $(\Delta x, \Delta y) \neq (w_x\tau, w_y\tau)$ due to the noise. The probability P_w is inversely proportional to SNR of the measurement and number of measurements made N_m. Therefore, qualitatively for a certain SNR there is a critical value N_{m0} such that for $N_m < N_{m0}$ most of the measurements are wrong, and for $N_m \gg N_{m0}$ measurement accuracy is high and does not improve significantly with increasing N_m. The critical value N_{m0} is inversely proportional to SNR.

To illustrate the principle, a simulation is performed. For $\mathbf{w} = (3, 0)$ and $k_{shot} = 0$ number of sensor measurement is $N_{fr} = [2, 20]$. The simulation is repeated for 100 turbulence realizations and $SNR = \{2.9, 25\}$. From the previous simulations it was observed that valid measurements are within 25% from the true wind velocity, and therefore all measurements outside this limit are considered wrong. For each value of frames taken, the valid measurements are counted and the probability P_{valid} of obtaining a valid measurement is plotted against number of frames taken in Figure 3-32. For settings with $P_{valid} > 90\%$ the variance of estimation is computed and represented in Figure 3-33.

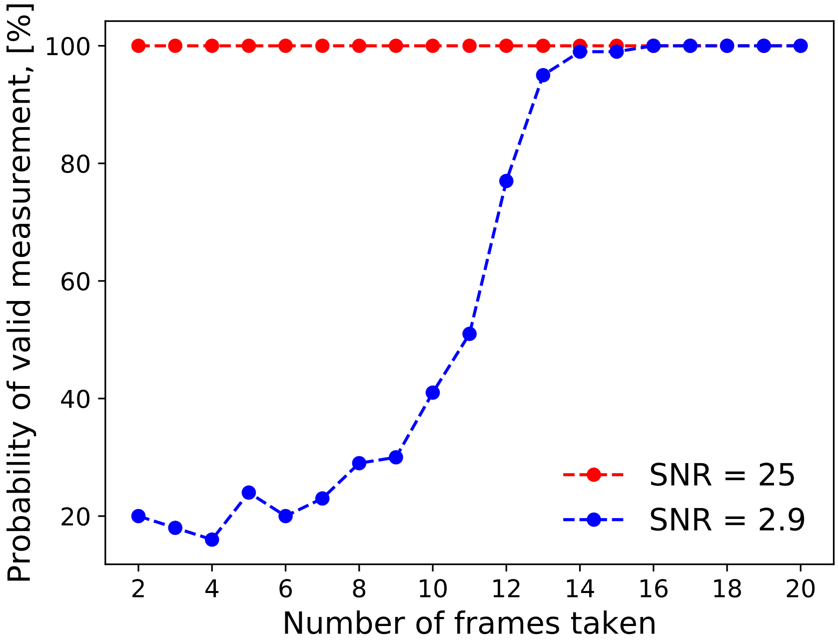

Figure 3-32: Probability of obtaining a correct measurement represented against the number of frames taken for two values of SNR.

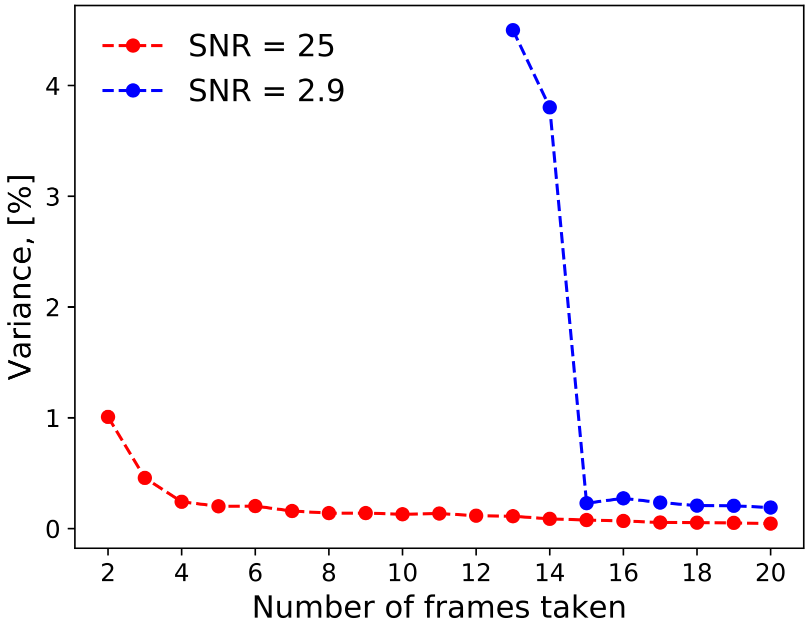

Figure 3-33: Variance of the measurement of the wind velocity for two SNR in the images taken, as a function of frames used for calculation.

The predicted behavior is observed: for $SNR = 25$ the estimator error is below 1% for all N_m, whereas for $SNR = 2.5$ only $N_m \geq 13$ can be used to obtain valid measurement with probability $P_{valid} > 90\%$. From Figure 3-33 it can be observed that estimator variance saturates quickly after reaching the critical N_m, and the saturated estimator variance is bellow 1% for both values of tested SNR. The result means that sensor bandwidth decreases significantly for lower SNR, but the measurement precision is much less sensitive to the light intensity.

The proposed method of wind velocity measurement was tested under perfect frozen flow assumption, which is to a certain extent unrealistic scenario. In real measurements the correlation peak does not only change its position with increasing τ, but its maximum is decreased and the width is increased. At certain critical τ_c the correlation peak is not observed anymore. Largest time delay between the measurements for which correlation is still observed τ_c is validity time of frozen flow assumption, which is estimated between $\tau_c = 40\,\text{ms}$ and several seconds [35]. Assume N_m measurements are made on a telescope of diameter d with a curvature sensor such that each pixel is conjugated to square $d_p\,\text{m} \times d_p\,\text{m}$. Assume additionally that wind velocity has only one component, $\mathbf{w} = (w_x, 0)$. The sampling period T_s is upper bounded by τ_c: $T_s < \frac{\tau_c}{N_m}$. Upped bound for wind velocity magnitude is given by

$$w_x < \frac{d}{2T_s} \tag{3-38}$$

$$w_x < \frac{dN_m}{2\tau_c}, \tag{3-39}$$

which is a statement that during one sampling period atmospheric layer must shift by $\Delta x < \frac{d}{2}$. The peak detection algorithm is able to estimate correlation peak positions $\Delta x \geq \Delta_{min}$ pixels, where $\Delta_{min} = 0.5$, therefore the smallest measurable wind velocity is

$$w_x \geq \frac{\Delta_{min} d_p}{T_s}, \tag{3-40}$$

$$w_x \geq \frac{N_m \Delta_{min} d_p}{\tau_c}. \tag{3-41}$$

For a telescope aperture diameter $d = 1\,\mathrm{m}$ conjugated to a curvature sensor of 256×256 pixels, assuming $T_s = 10\,\mathrm{ms}$ and $N_m = 10$ measurements, the wind velocity can be measured in interval $w_x \in [0.2, 50)\ \frac{\mathrm{m}}{\mathrm{s}}$.

A more realistic model of the atmosphere includes several superimposed turbulent layers with generally different Fried lengths and wind velocities. In this case, as reported by [31], the correlation maps contain several peaks. It is usually possible to distinguish one from another, and it is the matter of algorithmic processing of the correlation maps in case the peaks are too close. Here the use of the Curvature Sensor to obtain the higher resolution correlation maps is demonstrated. Testing the wind estimation performance of the CS using real astronomical measurements is of greater interest than the multilayer model. However, such data is not publicly available and is not easy to produce in the experimental conditions of this thesis.

Chapter 4

Results and conclusions

In this thesis Wavefront Curvature Sensor was studied and implemented in both simulations and real experimental setup. Theoretical aspects of Curvature Sensor (CS) were given, like Intensity Transport Equation and its validity conditions. Correction technique proposed by Roddier was implemented in optical schema used by Teague to retrieve wavefront curvature distribution. CS was first used with membrane Deformable Mirror. Measurements of influence matrix showed expected mainly diagonal structure with significant cross-talk present for boundary actuators. The sensor was used to correct aberrations with membrane mirror and the method was observed to diverge for general aberrations imitating a realistic scenario. CS was modified to include gradient measurements from Shack-Hartmann sensor for boundary actuators, and the method showed convergence. Upper bound for displacement distance between the CS cameras was derived for two types of mirror influence functions.

Next, the CS was operated with a high-order Deformable Mirror (DM) with 952 actuators. Influence matrix was measured again and the diagonal structure was observed. Adaptive Optics correction was performed and the method showed convergence without gradient measurements for boundary actuators, which was different from results of experiment with membrane DM. The results confirm that CS can potentially be used with very high order DMs when it is an issue to use Shack-Hartmann sensor.

Finally, an alternative application of CS was studied, namely wind velocity measurements. The method of correlation maps was used for the measurement, and the sensor demonstrated a high estimation accuracy and precision, even in case of noisy measurements. The sensor performance was evaluated only in simulations with frozen flow turbulence phase screen. Evaluating the sensor using real measurements from astronomical sites represents an interesting problem. The wind speed estimation can be more precise than in case of Shack-Hartmann (SH) again because the number of pixels of CS is much larger than the number of SH microlenses.

Bibliography

[1] H. W. Babcock, “The possibility of compensating astronomical seeing,” *Publications of the Astronomical Society of the Pacific*, vol. 65, no. 386, p. 229, 1953.

[2] V. P. Linnik, “On the Possibility of Reducing the Influence of Atmospheric Seeing on the Image Quality of Stars,” in *European Southern Observatory Conference and Workshop Proceedings* (F. Merkle, ed.), vol. 48 of *European Southern Observatory Conference and Workshop Proceedings*, p. 535, Jan. 1994.

[3] M. Born, E. Wolf, A. B. Bhatia, P. C. Clemmow, D. Gabor, A. R. Stokes, A. M. Taylor, P. A. Wayman, and W. L. Wilcock, *Principles of Optics: Electromagnetic Theory of Propagation, Interference and Diffraction of Light.* Cambridge University Press, 7 ed., 1999.

[4] R. Bracewell, *The Fourier Transform and its Applications.* Tokyo: McGraw-Hill Kogakusha, Ltd., second ed., 1978.

[5] J. Goodman, *Introduction to Fourier Optics.* McGraw-Hill physical and quantum electronics series, W. H. Freeman, 2005.

[6] E. Goulielmakis, M. Uiberacker, R. Kienberger, A. Baltuska, V. Yakovlev, A. Scrinzi, T. Westerwalbesloh, U. Kleineberg, U. Heinzmann, M. Drescher, and F. Krausz, “Direct measurement of light waves,” *Science*, vol. 305, no. 5688, pp. 1267–1269, 2004.

[7] M. R. Teague, “Deterministic phase retrieval: a green’s function solution,” *J. Opt. Soc. Am.*, vol. 73, pp. 1434–1441, Nov 1983.

[8] R. Tyson, *Principles of Adaptive Optics, Third Edition.* Series in Optics and Optoelectronics, CRC Press, 2010.

[9] F. Roddier, M. J. Northcott, J. E. Graves, D. L. McKenna, and D. Roddier, “One-dimensional spectra of turbulence-induced zernike aberrations: time-delay and isoplanicity error in partial adaptive compensation,” *J. Opt. Soc. Am. A*, vol. 10, pp. 957–965, May 1993.

[10] R. H. Freeman and J. E. Pearson, “Deformable mirrors for all seasons and reasons,” *Appl. Opt.*, vol. 21, pp. 580–588, Feb 1982.

[11] R. J. Noll, “Zernike polynomials and atmospheric turbulence∗,” *J. Opt. Soc. Am.*, vol. 66, pp. 207–211, Mar 1976.

[12] R. P. Grosso and M. Yellin, “The membrane mirror as an adaptive optical element∗,” *J. Opt. Soc. Am.*, vol. 67, pp. 399–406, Mar 1977.

[13] G. Vdovin and P. M. Sarro, “Flexible mirror micromachined in silicon,” *Appl. Opt.*, vol. 34, pp. 2968–2972, Jun 1995.

[14] J. M. Geary, *Introduction to wavefront sensors / Joseph M. Geary.* SPIE Optical Engineering Press Bellingham, Wash., USA, 1995.

[15] M. M. Vekshin, A. S. Levchenko, A. V. Nikitin, V. A. Nikitin, and N. A. Yacovenko, “Glass microlens arrays for shack–hartmann wavefront sensors,” *Measurement Science and Technology*, vol. 21, no. 5, p. 054010, 2010.

[16] M. Verhaegen and V. Verdult, *Filtering and System Identification: A Least Squares Approach.* New York, NY, USA: Cambridge University Press, 1st ed., 2007.

[17] F. Roddier, “Curvature sensing and compensation: a new concept in adaptive optics,” *Appl. Opt.*, vol. 27, pp. 1223–1225, Apr 1988.

[18] Q. Yang, C. Ftaclas, and M. Chun, “Wavefront correction with high-order curvature adaptive optics systems,” *J. Opt. Soc. Am. A*, vol. 23, pp. 1375–1381, Jun 2006.

[19] C. Campbell, “Wave-front sensing by use of a green’s function solution to the intensity transport equation: comment,” *J. Opt. Soc. Am. A*, vol. 24, pp. 2480–2481, Aug 2007.

[20] G. Vdovin, O. Soloviev, A. Samokhin, and M. Loktev, “Correction of low order aberrations using continuous deformable mirrors,” *Opt. Express*, vol. 16, pp. 2859–2866, Mar 2008.

[21] C. Ftaclas, A. Kellerer, and M. Chun, “Advanced Curvature Deformable Mirrors,” in *Advanced Maui Optical and Space Surveillance Technologies Conference*, p. E52, Sept. 2010.

[22] C. Ftaclas and A. Kostinski, “Curvature sensors, adaptive optics, and neumann boundary conditions,” *Appl. Opt.*, vol. 40, pp. 435–438, Feb 2001.

[23] F. Rigaut, B. L. Ellerbroek, and M. J. Northcott, “Comparison of curvature-based and shack–hartmann-based adaptive optics for the gemini telescope,” *Appl. Opt.*, vol. 36, pp. 2856–2868, May 1997.

[24] J. E. Graves, M. J. Northcott, F. J. Roddier, C. A. Roddier, D. Potter, D. J. O’Connor, F. J. Rigaut, and M. R. Chun, “First light for hokupa’a 36 on gemini north,” vol. 4007, pp. 4007 – 4007 – 5, 2000.

[25] V. G. Taranenko, G. P. Koshelev, and N. S. Romaniuk, “Local deformations of solid mirrors and their frequency dependence,” *Optiko Mekhanicheskaia Promyshlennost*, vol. 48, pp. 11–13, Nov. 1981.

[26] E. A. Sziklas and A. E. Siegman, "Diffraction calculations using fast fourier transform methods," *Proceedings of the IEEE*, vol. 62, pp. 410–412, March 1974.

[27] P. Gravel, G. Beaudoin, and J. A. D. Guise, "A method for modeling noise in medical images," *IEEE Transactions on Medical Imaging*, vol. 23, pp. 1221–1232, Oct 2004.

[28] J. Y. Wang and J. K. Markey, "Modal compensation of atmospheric turbulence phase distortion$*$," *J. Opt. Soc. Am.*, vol. 68, pp. 78–87, Jan 1978.

[29] OKO Tech, *96-channel deformable mirror with embedded electronics.*

[30] Boston Micromachines, *Mid-actuator count S-class DMs.*

[31] M. B. Roopashree, V. Akondi, and R. P. Budihala, "Real-time wind speed measurement using wavefront sensor data," vol. 7588, pp. 7588 – 7588 – 12, 2010.

[32] Z. Li and X. Li, "Fundamental performance of transverse wind estimator from shack-hartmann wave-front sensor measurements," *Opt. Express*, vol. 26, pp. 11859–11876, Apr 2018.

[33] M. Schöck and E. J. Spillar, "Measuring wind speeds and turbulence with a wavefront sensor," *Opt. Lett.*, vol. 23, pp. 150–152, Feb 1998.

[34] A. Beghi, A. Cenedese, and A. Masiero, "Multiscale phase screen synthesis based on local principal component analysis," *Appl. Opt.*, vol. 52, pp. 7987–8000, Nov 2013.

[35] Kellerer, A. and Tokovinin, A., "Atmospheric coherence times in interferometry: definition and measurement," *A&A*, vol. 461, no. 2, pp. 775–781, 2007.

Glossary

List of Acronyms

AO	Adaptive Optics
WF	Wavefront
WFS	Wavefront Sensor
SH	Shack-Hartmann
CS	Curvature Sensor
DM	Deformable Mirror
SLM	Spatial Light Modulator
ITE	Intensity Transport Equation